

WHAT MATTERS WHEN REPURPOSING DIFFUSION MODELS FOR GENERAL DENSE PERCEPTION TASKS?

Guangkai Xu Yongtao Ge Mingyu Liu Chengxiang Fan
 Kangyang Xie Zhiyue Zhao Hao Chen Chunhua Shen
 Zhejiang University

ABSTRACT

Extensive pre-training with large data is indispensable for downstream geometry and semantic visual perception tasks. Thanks to large-scale text-to-image (T2I) pretraining, recent works show promising results by simply fine-tuning T2I diffusion models for a few dense perception tasks. However, several crucial design decisions in this process still lack comprehensive justification, encompassing the necessity of the multi-step diffusion mechanism, training strategy, inference ensemble strategy, and fine-tuning data quality. In this work, we conduct a thorough investigation into critical factors that affect transfer efficiency and performance when using diffusion priors. Our key findings are: 1) High-quality fine-tuning data is paramount for both semantic and geometry perception tasks. 2) As a special case of the diffusion scheduler by setting its hyper-parameters, the multi-step generation can be simplified to a one-step fine-tuning paradigm without any loss of performance. 3) Apart from fine-tuning the diffusion model with only latent space supervision, task-specific supervision is beneficial to enhance fine-grained details. These observations culminate in the development of **GenPercept**, an effective deterministic one-step fine-tuning paradigm tailored for dense visual perception tasks exploiting diffusion priors. Different from the previous multi-step methods, our paradigm offers a much faster inference speed, and can be seamlessly integrated with customized perception decoders and loss functions for task-specific supervision, which can be critical for improving the fine-grained details of predictions. Comprehensive experiments on a diverse set of dense visual perceptual tasks, including monocular depth estimation, surface normal estimation, image segmentation, and matting, are performed to demonstrate the remarkable adaptability and effectiveness of our proposed method.

1 INTRODUCTION

Recent studies have explored the transferability of text-to-image (T2I) diffusion models to dense visual perception tasks, such as geometry estimation (Ke et al., 2024; Lee et al., 2024; Fu et al., 2024b; Gui et al., 2024; Ye et al., 2024), image segmentation (Van Gansbeke & De Brabandere, 2024; Lee et al., 2024), and inverse rendering (Chen et al., 2024; Kocsis et al., 2024; Zeng et al., 2024). While these works have demonstrated impressive results by repurposing diffusion models for estimating geometric and semantic dense prediction maps, the critical design choices made in transferring diffusion models to other dense perception tasks still lack comprehensive justification. This makes it challenging to determine the optimal strategy for achieving optimal performance.

For example, Ke et al. (2024) align the visual perception process with the denoising process of Stable Diffusion by fine-tuning all U-Net parameters. They highlight the significance of “multi-resolution noise” in the forward diffusion process during training, aiming to obtain clean predictions by gradually removing Gaussian noise. On the other hand, Lee et al. (2024) modify the forward diffusion process by interpolating perception annotations with RGB images instead of using Gaussian noise, and only train the low-rank adaptation (LoRA) (Hu et al., 2022) parameters while keeping the U-Net frozen. To our knowledge, the effective components of these approaches have not been thoroughly investigated, and it is unclear which design choices contribute most to the success.

arXiv:2403.06090v4 [cs.CV] 1 Dec 2024

In this work, we examine the design space of repurposing diffusion models for dense visual perception tasks, and attempt to answer the key question: **What are the important design choices when adapting diffusion models for general dense perception tasks?**

To answer this question, we rethink the importance of both fine-tuning protocols and fine-tuning data. From the perspective of fine-tuning protocols, we categorize recent methods into two main groups: *stochastic multi-step generation* and *deterministic multi-step generation*. We explore several critical design choices, including the diffusion mechanism, key architectural components, training methodologies, and data quality. Our key observations are as follows: **1)** By setting the hyperparameters of the diffusion scheduler to particular values, the multi-step generation can be simplified to a one-step fine-tuning paradigm without any loss of performance. **2)** Strict adherence to traditional diffusion processes appears to be unnecessary. Single-step inference provides similar performance with significantly faster execution. **3)** High-quality synthetic fine-tuning data is crucial for several perception tasks. From the perspective of fine-tuning data quality, we conduct comprehensive dataset ablation studies on both synthetic datasets and real-world datasets.

Based on the aforementioned observations, we propose **GenPercept** (see Fig. 1), a deterministic fine-tuning paradigm featuring a remarkably simple one-step inference pipeline, an optional customized decoder, and an easily adaptable pixel-wise loss. We conduct extensive quantitative and qualitative experiments on a wide range of visual dense perception tasks, including monocular depth estimation, surface normal estimation, image segmentation, and matting to demonstrate the effectiveness and generalization capability of our method.

In conclusion, our contributions can be summarized as follows: **1)** We systematically analyze the design space of fine-tuning protocols, considering both model architecture and dataset selection, through comprehensive ablation studies. **2)** Based on these insights, we propose GenPercept, a simple paradigm that harnesses the power of the pre-trained UNet from diffusion models for generalizable dense visual perception tasks.

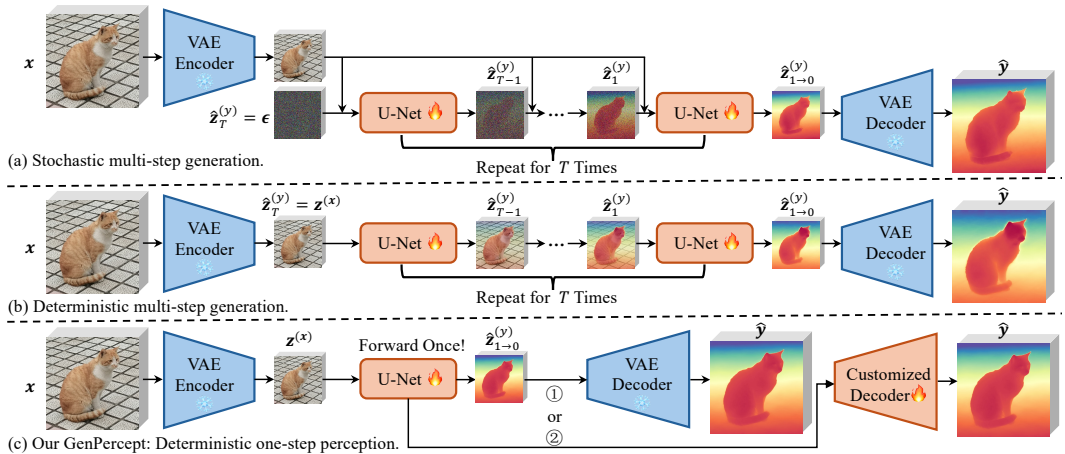


Figure 1: Comparisons of three different pipelines. Our GenPercept enables one-step inference and supports pixel-wise losses and customized decoders to replace the cumbersome VAE decoder. We also extend GenPercept to five dense perception tasks including monocular depth estimation, surface normal estimation, dichotomous image segmentation, semantic segmentation, and image matting.

2 PRELIMINARY

We take the latent diffusion model as an example. To model the data distribution, the idea of the diffusion model (Rombach et al., 2022; Chen et al., 2023; Song et al., 2020; Ho et al., 2020) is to randomly sample a noise $\mathbf{z}_T^{(y)} \sim \mathcal{N}(\mathbf{0}, \mathbf{I})$ and sequentially denoise it into a $\mathbf{z}_0^{(y)}$, which is distributed according to the data. In the forward diffusion process, $\mathbf{z}_t^{(y)}$ is sampled by $\mathbf{z}_t^{(y)} = \sqrt{\bar{\alpha}_t} \mathbf{z}^{(y)} + \sqrt{1 - \bar{\alpha}_t} \epsilon$, where $\epsilon \sim \mathcal{N}(\mathbf{0}, \mathbf{I})$, and $\bar{\alpha}_t = \prod_{s=1}^t (1 - \beta_s)$. The variance schedule $\{\beta_t \in (0, 1)\}_{t=1}^T$ is

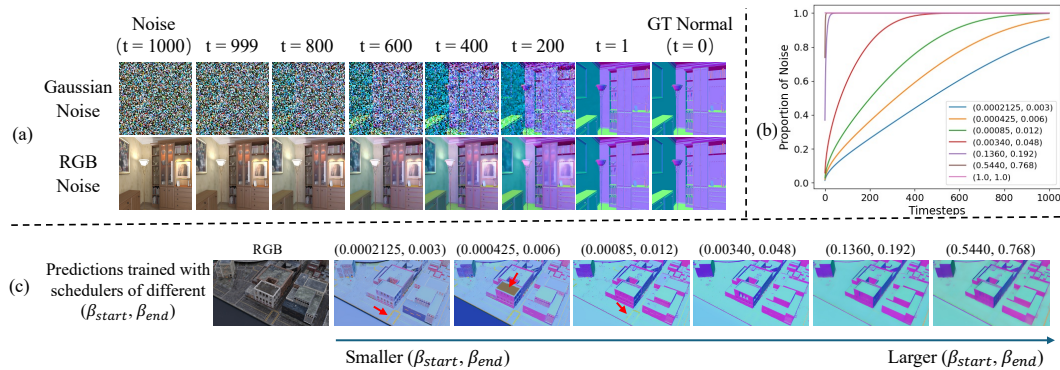


Figure 2: Illustration of different noise forms and proportions in the forward diffusion process. (a) Visualization of interpolating ground-truth labels with Gaussian noise and RGB noise. (b) The relationship between the noise proportion $\sqrt{\bar{\alpha}_t}$ and the $(\beta_{start}, \beta_{end})$ hyperparameters. (c) Small $(\beta_{start}, \beta_{end})$ values during the training of deterministic multi-step generation tend to lead to unclean estimation, which contains some RGB information. Enlarging them may alleviate this issue.

interpolated between β_{start} and β_{end} with T steps, where larger values of $(\beta_{start}, \beta_{end})$ correspond to smaller $\bar{\alpha}_t$ values, *i.e.*, smaller proportion of noise. In the reverse process, Salimans & Ho (2021) use a “v-prediction” objective, where a denoiser v_θ minimizes the following:

$$\mathcal{L} = \mathbb{E}_{\mathbf{z}^{(y)}, \epsilon \sim \mathcal{N}(0, I), t \sim \mathcal{U}(T)} \left\| (\sqrt{\bar{\alpha}_t} \epsilon - \sqrt{1 - \bar{\alpha}_t} \mathbf{z}^{(y)}) - v_\theta(\mathbf{z}_t, t) \right\|_2^2. \quad (1)$$

To fully leverage the pre-trained prior of the diffusion models for dense prediction tasks, previous works have reformulated these tasks as a multi-step denoising process, especially on monocular depth estimation. Given a data pair $(\mathbf{z}^{(x)}, \mathbf{z}^{(y)})$ where $\mathbf{z}^{(x)}$ is the observation and $\mathbf{z}^{(y)}$ is the prediction target, *stochastic multi-step generation* methods (Ke et al., 2024; Fu et al., 2024b; Gui et al., 2024) such as Marigold (Ke et al., 2024) add $\mathbf{z}^{(x)}$ as an additional input to the denoiser v_θ , and use $v_\theta(\mathbf{z}_t^{(y)}, \mathbf{z}^{(x)}, t)$ to predict $\mathbf{z}^{(y)}$. By contrast, *deterministic multi-step generation* methods such as DMP (Lee et al., 2024) take the observation $\mathbf{z}^{(x)}$ as a deterministic noise and compose $\mathbf{z}_t^{(y)}$ as a blend between $\mathbf{z}^{(x)}$ and $\mathbf{z}^{(y)}$:

$$\mathbf{z}_t = \mathbf{z}_t^{(y)} = \sqrt{\bar{\alpha}_t} \mathbf{z}^{(y)} + \sqrt{1 - \bar{\alpha}_t} \mathbf{z}^{(x)}, \quad t = [1, \dots, T], \quad (2)$$

The denoising process and forward diffusion process of these two categories are illustrated in Fig. 1 and Fig. 2 (a). We offer detailed formulations in the supplementary material.

3 DIFFUSION MODELS FOR VISUAL PERCEPTION TASKS

In this section, we explore the necessity and highlight the findings of the multi-step diffusion mechanism, the architectural components, training strategy, and fine-tuning data quality. We select the stochastic method Marigold (Ke et al., 2024) and the deterministic method DMP (Lee et al., 2024) as our baseline methods. The default experimental setting here is similar to Ke et al. (2024) and can be found in the supplementary material.

3.1 THE FORM AND PROPORTION OF NOISE IN THE FORWARD DIFFUSION PROCESS

For the training process of Marigold and DMP, the timestep t is sampled to control the proportion of noise added to the ground truth, and the network is trained to recover a clean ground truth from a noisy latent. For smaller timesteps such as “ $t = 200$ ”, as illustrated in Fig. 2(a), the input to the network retains significant ground truth information (*e.g.*, the purple color of the normal). Therefore, we hypothesize that *a certain level of ground-truth label information being part of the input* makes

Table 1: Comprehensive quantitative comparisons about the impact of noise forms and proportions in the forward diffusion process on monocular depth estimation. Visualizations of different noise forms and the effect of $(\beta_{start}, \beta_{end})$ values are shown in Fig. 2. The performance of DMP improves steadily, while Marigold shows initial improvements followed by a decline. When β_{start} and β_{end} are equal to 1, the inference process can be reduced to one step without compromising performance. “Rank” means the average rank of ten evaluation performance (smaller is better).

Type	Noise Form	Multi-res Noise	Steps	$(\beta_{start}, \beta_{end})$	KITTI		NYU		ScanNet		DIODE		ETH3D		Rank↓	
					AbsRel↓	$\delta_1\uparrow$	AbsRel↓	$\delta_1\uparrow$	AbsRel↓	$\delta_1\uparrow$	AbsRel↓	$\delta_1\uparrow$	AbsRel↓	$\delta_1\uparrow$		
baseline	Marigold	Gaussian	✓	10	(0.0002125, 0.003)	0.358	0.462	0.297	0.555	0.246	0.625	0.494	0.565	0.267	0.640	7.0
	Marigold	Gaussian	✓	10	(0.000425, 0.006)	0.122	0.854	0.106	0.887	0.136	0.829	0.345	0.716	0.086	0.927	5.8
	Marigold	Gaussian	✓	10	(0.00085, 0.012)	0.099	0.909	0.063	0.956	0.075	0.937	0.316	0.764	0.075	0.947	3.6
	Marigold	Gaussian	✓	10	(0.0034, 0.048)	0.100	0.906	0.057	0.963	0.063	0.957	0.308	0.768	0.074	0.948	2.3
	Marigold	Gaussian	✓	10	(0.1360, 0.192)	0.119	0.861	0.058	0.963	0.061	0.961	0.315	0.760	0.073	0.950	2.8
	Marigold	Gaussian	✓	10	(0.5440, 0.768)	0.124	0.852	0.060	0.961	0.064	0.958	0.322	0.749	0.079	0.943	4.7
Marigold	Gaussian	✓	10	(1.0, 1.0)	0.104	0.897	0.055	0.965	0.059	0.962	0.312	0.762	0.069	0.955	1.7	
Marigold	Gaussian	✓	1	(1.0, 1.0)	0.104	0.897	0.055	0.965	0.059	0.962	0.312	0.762	0.069	0.955	-	
baseline	Marigold	Gaussian	×	10	(0.0002125, 0.003)	0.587	0.255	0.337	0.490	0.257	0.604	0.600	0.469	0.372	0.503	7.0
	Marigold	Gaussian	×	10	(0.000425, 0.006)	0.536	0.289	0.313	0.527	0.248	0.621	0.565	0.499	0.328	0.575	6.0
	Marigold	Gaussian	×	10	(0.00085, 0.012)	0.153	0.807	0.162	0.802	0.187	0.737	0.411	0.641	0.157	0.826	5.0
	Marigold	Gaussian	×	10	(0.0034, 0.048)	0.101	0.907	0.058	0.963	0.066	0.954	0.309	0.765	0.074	0.950	2.4
	Marigold	Gaussian	×	10	(0.1360, 0.192)	0.115	0.870	0.056	0.965	0.060	0.961	0.313	0.763	0.072	0.953	2.3
	Marigold	Gaussian	×	10	(0.5440, 0.768)	0.124	0.848	0.059	0.963	0.063	0.958	0.318	0.752	0.077	0.946	3.7
Marigold	Gaussian	×	10	(1.0, 1.0)	0.102	0.901	0.054	0.966	0.059	0.962	0.312	0.762	0.071	0.955	1.5	
Marigold	Gaussian	×	1	(1.0, 1.0)	0.102	0.901	0.054	0.966	0.059	0.962	0.312	0.762	0.071	0.955	-	
baseline	DMP	RGB	×	10	(0.0002125, 0.003)	0.476	0.336	0.267	0.601	0.216	0.677	0.457	0.588	0.185	0.757	6.9
	DMP	RGB	×	10	(0.000425, 0.006)	0.265	0.630	0.201	0.072	0.195	0.717	0.386	0.674	0.116	0.880	6.1
	DMP	RGB	×	10	(0.00085, 0.012)	0.134	0.837	0.117	0.871	0.147	0.808	0.353	0.721	0.093	0.919	5.0
	DMP	RGB	×	10	(0.0034, 0.048)	0.107	0.890	0.077	0.939	0.087	0.923	0.318	0.766	0.078	0.940	3.8
	DMP	RGB	×	10	(0.1360, 0.192)	0.107	0.890	0.063	0.959	0.068	0.955	0.305	0.773	0.073	0.948	2.2
	DMP	RGB	×	10	(0.5440, 0.768)	0.106	0.897	0.061	0.959	0.066	0.952	0.309	0.768	0.075	0.945	2.3
DMP	RGB	×	10	(1.0, 1.0)	0.100	0.902	0.053	0.966	0.059	0.961	0.309	0.768	0.068	0.956	1.2	
Our baseline	RGB	×	1	(1.0, 1.0)	0.100	0.902	0.053	0.966	0.059	0.961	0.309	0.768	0.068	0.956	-	

the network comparatively be easier to recover the clean ground truth latent than the case of the absence of any ground truth information during training. This can limit the network’s capacity to learn comprehensive knowledge and lead to unsatisfactory performance, as it is known that networks can become lazy that tend to exploit “shortcuts”—the ground truth labels in the input in our case. On the other hand, for inference there is no such ground truth available, causing disparity of input signals between inference and training. We note that T2I tasks may suffer less due to their stochastic nature, namely, converting a text prompt to a generated image is one-to-many mapping process.

To alleviate this issue, we attempt to control the blending proportion by changing the $(\beta_{start}, \beta_{end})$ values of the diffusion model’s DDPM scheduler. As shown in Fig. 2(b) and Fig. 2 of the supplementary, training with a $(\beta_{start}, \beta_{end})$ value of (1.0, 1.0) achieves the best rank performance for both Gaussian noise and RGB noise, which is demonstrated in Table 1. Rather than achieving consistent performance improvement while increasing the noise proportion, we observed that Marigold’s performance begins to be slightly unstable when the $(\beta_{start}, \beta_{end})$ values are sufficiently high. Experiments of varying the random seed during both the training and inference process are conducted to rule out the influence of randomness. The results show that we may not be able to exactly find a set of unique values for $(\beta_{start}, \beta_{end})$ to achieve the best accuracy, as the final accuracy can be affected by a few other factors besides the aforementioned one.

Additionally, when $(\beta_{start}, \beta_{end})$ are equal to 1, the noise proportion $\sqrt{\bar{\alpha}_t}$ is equal to 0, and the formulation of DMP can be derived from Eq. (1) and Eq. (8) as follows.

$$\mathbf{z}_t = \mathbf{z}_t^{(\mathbf{y})} = \sqrt{\bar{\alpha}_t} \mathbf{z}^{(\mathbf{y})} + \sqrt{1 - \bar{\alpha}_t} \mathbf{z}^{(\mathbf{x})} = \mathbf{z}^{(\mathbf{x})}, \quad t = [1, \dots, T],$$

$$\mathcal{L} = \mathbb{E}_{\mathbf{z}^{(\mathbf{y})}, \epsilon \sim \mathcal{N}(0, I), t \sim U(T)} \left\| -\mathbf{z}^{(\mathbf{y})} - \mathbf{v}_\theta(\mathbf{z}_t, t) \right\|_2^2. \quad (3)$$

In this case, the output of the denoiser $\mathbf{v}_\theta(\cdot, \cdot)$ is enforced to learn the negative value of the ground truth latent for each step, and the multi-step denoising is equivalent to the single-step denoising. We propose to reduce the DDIM steps of DMP to one and call it “deterministic one-step perception”. The resulting inference can be significantly faster, with performance remaining almost unchanged. We name this as “our baseline” for the subsequent analysis.

Finding 1. By setting the $(\beta_{start}, \beta_{end})$ values to 1, the multi-step generation is simplified to a one-step fine-tuning paradigm without any loss of performance in both stochastic and deterministic methods, e.g., Marigold (Ke et al., 2024) and DMP (Lee et al., 2024) respectively.

3.2 WHERE DOES THE RICH VISUAL KNOWLEDGE RESIDE IN DIFFUSION MODELS?

Based on the baseline we proposed in §3.1, we conduct detailed ablation studies to thoroughly investigate the necessity of each component of Stable Diffusion. Results are reported in Table 2.

Table 2: Explorations on the impact of the Stable Diffusion components on depth estimation. Customized decoders and losses can also enable inference acceleration and performance improvement.

Setting	Loss	KITTI		NYU		ScanNet		DIODE		ETH3D	
		AbsRel↓	δ_1 ↑	AbsRel↓	δ_1 ↑	AbsRel↓	δ_1 ↑	AbsRel↓	δ_1 ↑	AbsRel↓	δ_1 ↑
Our baseline	MSE (Latent)	0.100	0.902	0.053	0.966	0.059	0.961	0.309	0.768	0.068	0.956
Train U-Net from scratch	MSE (Latent)	0.219	0.650	0.186	0.736	0.183	0.729	0.426	0.614	0.185	0.741
Train VAE decoder from scratch	MSE (Image)	0.096	0.916	0.055	0.964	0.058	0.964	0.302	0.759	0.071	0.950
Baseline + Image MSE loss	MSE (Image)	0.097	0.915	0.054	0.964	0.059	0.964	0.305	0.760	0.071	0.953
Baseline + Image customized loss	MSE + SSI + Grad. (Image)	0.094	0.923	0.052	0.966	0.056	0.965	0.302	0.767	0.066	0.967
Train DPT decoder from scratch	MSE (Image)	0.099	0.912	0.055	0.964	0.058	0.963	0.302	0.759	0.069	0.956

Denoisier. We reinitialize the U-Net parameters and train the network from scratch on the same datasets. Without prior knowledge of large data from LAION-5B, the network performs poorly and loses the generalization capability. This indicates that most of the prior knowledge is stored in the U-Net module.

VAE AutoEncoder. The VAE encoder’s original architecture is kept intact to maintain the consistency of the encoding process. For the VAE decoder, we train it from scratch with image pixel MSE loss. Without pre-trained parameters of the VAE decoder, it still performs well.

Customized Head and Loss. The deterministic one-step perception pipeline enables customized heads and loss functions. By utilizing a DPT decoder (Ranftl et al., 2021) and the loss functions of DepthAnythingv2 (Yang et al., 2024b), we can implement a lightweight decoder that supervises pixel-wise information at a higher resolution rather than latent features at 1/8 resolution. This approach can accelerate inference times and enhance the acquisition of fine-grained details.

Finding 2. The primary perceptual prior knowledge of diffusion models is encapsulated within the U-Net of the diffusion model. Customized heads and loss functions offers flexibility and may lead to faster inference speed and improved results.

3.3 WHAT ABOUT THE TIMESTEPS AND TEXT PROMPTS?

The timesteps and text prompts are crucial elements in utilizing the Stable Diffusion model to generate diverse images. We conducted ablation studies to investigate their significance. The results reported in Table 3 indicate a negligible difference between various settings. Owing to the inherent certainty associated with visual perception tasks, the diversity typically offered by the textual inputs appears to be unnecessary. Similarly, the utility of timesteps is reduced, as the single-step paradigm does not require progressive denoising.

Table 3: Quantitative comparisons among different timesteps and text prompts on depth estimation.

Setting	Text Prompt	Train / Infer Timesteps	KITTI		NYU		ScanNet		DIODE		ETH3D	
			AbsRel↓	δ_1 ↑	AbsRel↓	δ_1 ↑	AbsRel↓	δ_1 ↑	AbsRel↓	δ_1 ↑	AbsRel↓	δ_1 ↑
Our baseline	****	Random / 1	0.100	0.902	0.053	0.966	0.059	0.961	0.309	0.768	0.068	0.956
Valid text input	"A high quality RGB image"	Random / 1	0.101	0.900	0.053	0.967	0.058	0.964	0.312	0.762	0.070	0.954
Random text input	"*F3@qV!k2*#Zp*n%lLz"	Random / 1	0.099	0.904	0.054	0.965	0.059	0.963	0.311	0.763	0.069	0.955
Timestep1	****	1 / 1	0.100	0.906	0.054	0.965	0.060	0.961	0.304	0.769	0.069	0.956
Timestep500	****	500 / 500	0.102	0.897	0.053	0.966	0.059	0.961	0.307	0.765	0.068	0.956
Timestep900	****	900 / 900	0.105	0.891	0.054	0.966	0.058	0.964	0.309	0.762	0.068	0.953

Finding 3. The timesteps and text prompts of diffusion models are negligible for the performance of visual perception tasks.

3.4 HOW TO LEVERAGE THE U-NET’S PRIOR KNOWLEDGE?

The significance of the denoisier cannot be overstated. However, the strategies for its utilization are worth a careful study. Should we freeze the denoisier, utilize its intermediate features, and merely

Table 4: Explorations on the paradigms to leverage U-Net’s prior knowledge on depth estimation.

Setting	LoRA Rank	KITTI		NYU		ScanNet		DIODE		ETH3D	
		AbsRel↓	δ_1 ↑	AbsRel↓	δ_1 ↑	AbsRel↓	δ_1 ↑	AbsRel↓	δ_1 ↑	AbsRel↓	δ_1 ↑
Our baseline	-	0.100	0.902	0.053	0.966	0.059	0.961	0.309	0.768	0.068	0.956
Freeze U-Net + Train DPT decoder	-	0.144	0.803	0.086	0.931	0.097	0.911	0.309	0.768	0.068	0.956
Train U-Net with LoRA	4	0.211	0.644	0.095	0.914	0.100	0.902	0.372	0.689	0.121	0.864
Train U-Net with LoRA	16	0.166	0.746	0.085	0.931	0.087	0.927	0.352	0.712	0.104	0.901
Train U-Net with LoRA	64	0.138	0.817	0.077	0.944	0.079	0.940	0.336	0.734	0.089	0.930
Train U-Net with LoRA	256	0.133	0.827	0.069	0.952	0.073	0.947	0.325	0.745	0.088	0.933
Train U-Net with LoRA	1024	0.125	0.849	0.067	0.955	0.074	0.947	0.324	0.747	0.084	0.939

Table 5: Investigations into the impact of training data quality on depth estimation.

Data Quality	Datasets	KITTI		NYU		ScanNet		DIODE		ETH3D	
		AbsRel↓	δ_1 ↑	AbsRel↓	δ_1 ↑	AbsRel↓	δ_1 ↑	AbsRel↓	δ_1 ↑	AbsRel↓	δ_1 ↑
Synthetic Data	Hypersim (50K) + Virtual KITTI (40K)	0.100	0.902	0.053	0.966	0.059	0.961	0.309	0.768	0.068	0.956
Real Data	Taskonomy (50K) + Cityscapes (40K)	0.123	0.857	0.055	0.966	0.062	0.958	0.293	0.762	0.074	0.947

fine-tune the decoder for specific tasks? Alternatively, can we employ LoRA (Hu et al., 2022) instead of extensively fine-tuning the entire denoiser? Unfortunately, the evidence suggests that neither approach is ideal. As illustrated in Table 4, freezing the denoiser significantly compromises performance. Although incorporating LoRA offers some advantages, it may not fully leverage the potential of denoiser, especially with regular LoRA ranks of 4 and 16. This limitation likely stems from the substantial differences between the noise-to-image denoising process and the image-to-perception prediction task.

Finding 4. Fine-tuning the denoiser appears to be preferable for achieving better results, compared to either merely utilizing its intermediate features or training a LoRA.

3.5 IS THE TRAINING DATA QUALITY ESSENTIAL?

The quality of annotations in real datasets is often lower compared to synthetic datasets, where data is precisely rendered via simulators. In Table 5, we explore the impact of data quality on the fine-tuning process. We sample the same distribution of real data, consisting of 90% from approximately 50K indoor images from the Taskonomy dataset (Zamir et al., 2018) and 10% from about 40K outdoor images from the Cityscapes dataset (Cordts et al., 2016). With lower annotation quality, the model achieves slightly worse performance. Also, the visualization in the supplementary material indicates that noisy data significantly influences detailed predictions in visual perception tasks.

Finding 5. Data quality affects the fine-grained details of dense predictions significantly.

3.6 SUMMARY OF THE OBERVATIONS

Based on the preceding analysis, an effective approach to leveraging the prior knowledge of diffusion models is to use them as single-step deterministic perception estimators. This can be done with either a VAE decoder or a customized lightweight decoder. Additionally, employing pixel-specific customized losses can further enhance detail and overall performance. We compare our deterministic single-step perception method with previous multi-step paradigms in Fig. 1. In the following section, we extend these findings to a broader set of visual perception tasks, including surface normal estimation, semantic image segmentation, dichotomous image segmentation, and image matting.

4 EXPERIMENTS ON VARIOUS DENSE VISUAL PERCEPTUAL TASKS

In this section, we empirically show the robust transfer ability of our GenPercept on diverse visual tasks. Unless specified otherwise, we freeze the VAE AutoEncoder and fine-tune the U-Net of Stable Diffusion v2.1 to estimate the ground-truth label latent for 30000 iterations, with a resolution of (768, 768), a batch size of 32, and a learning rate of 3e-5. Different customized loss functions are utilized to improve the performance further on dense visual perception tasks.

Table 6: Quantitative comparison of affine-invariant depth estimation on five zero-shot datasets. Part of the reported results ([†]) are evaluated following the evaluation protocol of Marigold by ourselves.

Method	Training Samples	KITTI		NYU		ScanNet		DIODE		ETH3D	
		AbsRel _↓	δ_1 _↑	AbsRel _↓	δ_1 _↑	AbsRel _↓	δ_1 _↑	AbsRel _↓	δ_1 _↑	AbsRel _↓	δ_1 _↑
MiDaS (Ranftl et al., 2020)	2M	0.236	0.630	0.111	0.885	0.121	0.846	0.332	0.715	0.184	0.752
OmniData (Eftekhari et al., 2021)	12.2M	0.149	0.835	0.074	0.945	0.075	0.936	0.339	0.742	0.166	0.778
DPT-large (Ranftl et al., 2021)	1.4M	0.100	0.901	0.098	0.903	0.082	0.934	0.182	0.758	0.078	0.946
DepthAnything [†] (Yang et al., 2024a)	63.5M	0.080	0.946	0.043	0.980	0.043	0.981	0.261	0.759	0.058	0.984
DepthAnything v2 [†] (Yang et al., 2024b)	62.6M	0.080	0.943	0.043	0.979	0.042	0.979	0.321	0.758	0.066	0.983
Metric3D v2 [†] (Hu et al., 2024)	16M	0.052	0.979	0.039	0.979	0.023	0.989	0.147	0.892	0.040	0.983
DiverseDepth (Yin et al., 2020)	320K	0.190	0.704	0.117	0.875	0.109	0.882	0.376	0.631	0.228	0.694
LDReS (Yin et al., 2021)	354K	0.149	0.784	0.090	0.916	0.091	0.917	0.271	0.766	0.171	0.777
HDN (Zhang et al., 2022)	300K	0.115	0.867	0.069	0.948	0.080	0.939	0.246	0.780	0.121	0.833
GeoWizard (Fu et al., 2024b)	280K	0.097	0.921	0.052	0.966	0.061	0.953	0.297	0.792	0.064	0.961
DepthFM (Gui et al., 2024)	63K	0.083	0.934	0.065	0.956	-	-	0.225	0.800	-	-
Marigold [†] (Ke et al., 2024)	74K	0.099	0.916	0.055	0.964	0.064	0.951	0.308	0.773	0.065	0.960
DMP Official [†] (Lee et al., 2024)	-	0.240	0.622	0.109	0.891	0.146	0.814	0.361	0.706	0.128	0.857
GeoWizard [†] (Fu et al., 2024b)	280K	0.129	0.851	0.059	0.959	0.066	0.953	0.328	0.753	0.077	0.940
DepthFM [†] (Gui et al., 2024)	63K	0.174	0.718	0.082	0.932	0.095	0.903	0.334	0.729	0.101	0.902
Our GenPercept (Depth)	90K	0.094	0.923	0.052	0.966	0.056	0.965	0.302	0.767	0.066	0.957
Our GenPercept (Disparity)	90K	0.080	0.934	0.058	0.969	0.063	0.960	0.226	0.741	0.096	0.959
Our GenPercept (Disparity + DPT head)	90K	0.078	0.935	0.059	0.967	0.064	0.961	0.228	0.740	0.094	0.961

Table 7: Quantitative comparison of surface normal estimation on three zero-shot datasets. We evaluate mean error_↓, median error_↓ (med.), and the percentages of pixels_↑ with five thresholds. Part of the reported results ([†]) are evaluated following the evaluation protocol of DSINE by ourselves.

Method	Training Samples	NYU v2										ScanNet					Sintel					
		mean	med.	5.0°	7.5°	11.25°	22.5°	30°	mean	med.	5.0°	7.5°	11.25°	22.5°	30°	mean	med.	5.0°	7.5°	11.25°	22.5°	30°
OmniData v1 (Eftekhari et al., 2021)	12.2M	23.1	12.9	21.6	33.4	45.8	66.3	73.6	22.9	12.3	21.5	34.5	47.4	66.1	73.2	41.5	35.7	3.0	5.8	11.4	30.4	42.0
Omnidata v2 (Kar et al., 2022)	12.2M	17.2	9.7	25.3	40.2	55.5	76.5	83.0	16.2	8.5	29.1	44.9	60.2	79.5	84.7	40.5	35.1	4.6	7.9	14.7	33.0	43.5
Metric3D v2 [†] (Hu et al., 2024)	8.8M	13.5	6.7	40.1	53.5	65.9	82.6	87.7	11.8	5.5	46.6	60.7	71.6	85.4	89.7	22.8	14.2	18.4	28.5	41.6	66.7	75.8
Geowizard (Fu et al., 2024b)	280K	17.0	-	-	-	56.5	-	-	15.4	-	-	-	61.6	-	-	-	-	-	-	-	-	-
DINSE [†] (Bae & Davison, 2024a)	160K	16.4	8.4	32.8	46.3	59.6	77.7	83.5	16.2	8.3	29.8	45.9	61.0	78.7	84.4	34.9	28.1	8.9	14.1	21.5	41.5	52.7
Geowizard [†] (Fu et al., 2024b)	280K	19.8	11.2	18.0	32.7	50.2	73.0	79.9	21.1	11.9	15.9	29.7	47.4	70.7	77.8	36.1	28.4	4.1	8.6	16.9	39.8	52.5
Our GenPercept (Latent MSE loss)	90K	17.4	9.5	23.3	40.0	56.3	76.8	83.0	16.3	8.9	25.8	42.7	59.6	79.4	84.8	44.4	31.6	3.4	7.5	15.0	37.0	48.0
Our GenPercept (Image angular loss)	90K	16.4	8.0	33.3	47.8	60.9	78.3	83.7	15.2	7.4	33.9	50.7	65.0	80.9	85.7	34.6	26.2	5.2	9.8	18.4	43.8	55.8

4.1 GEOMETRIC ESTIMATION

For geometry evaluation, the ensemble size, inference resolution, valid evaluation depth range (specific for depth estimation), and evaluation average paradigm (average by pixels or average by the number of images) can be different for each method. To compare these approaches fairly, we follow the open-source evaluation code of Marigold (Ke et al., 2024) for depth and DSINE (Bae & Davison, 2024a) for surface normal, and evaluate the performance of partial existing SOTA methods with their officially released model weights. They are labeled with [†] in the Table.

Monocular Depth Estimation. The monocular depth estimation aims to predict the vertical distance between the observed object and the camera from an RGB image. The estimated depth is formulated as affine-invariant depth (Yin et al., 2021; Ranftl et al., 2020; 2021), and should be recovered by performing least square regression with the ground truth. The evaluation is performed on five zero-shot datasets including KITTI (Geiger et al., 2013), NYU (Silberman et al., 2012), ScanNet (Dai et al., 2017), DIODE (Vasiljevic et al., 2019), and ETH3D (Schops et al., 2017). We compute the absolute relative error (AbsRel_↓) and percentage of accurate valid depth pixels (δ_1 _↑). Invalid regions are filtered out and the metrics are averaged on all images.

Surface Normal Estimation. The surface normal estimation aims to predict a vector perpendicular to tangent plane of the surface at each point P, which represents the orientation of the object’s surface. For evaluation, we compute the angular error on three zero-shot datasets including NYU (Silberman et al., 2012), ScanNet (Dai et al., 2017), and Sintel (Butler et al., 2012). The mean_↓, median_↓, and the percentages of pixels_↑ with error below thresholds [5°, 7.5°, 11.25°, 22.5°, 30°] are reported. Invalid regions are filtered out and the metrics are averaged on all images.

Quantitative Evaluation. Quantitative results on monocular depth estimation and surface normal estimation are shown in Table 6 and Table 7, respectively. Even trained on limited synthetic datasets only, our GenPercept shows much robustness and achieves promising performance on diverse unseen scenes. For monocular depth models, we train them with pixel-wise MSE loss, scale-shift-invariant loss (Ranftl et al., 2020), and gradient loss (Ranftl et al., 2020). Furthermore, our disparity

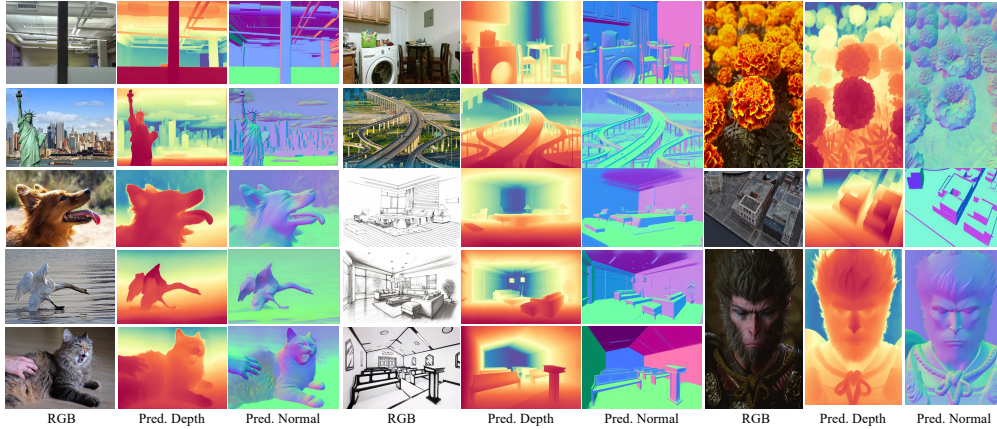


Figure 3: Qualitative results of monocular depth and surface normal estimation. The model works surprisingly well on *out-of-domain images (sketch and cartoon images)*.

model (inverse of the depth) shows much better performance on datasets with outdoor scenes, such as KITTI and DIODE, but less performance on indoor datasets. Therefore, we suggest adopting the depth model for indoor scenes and the disparity model for outdoor scenes experimentally. By replacing the VAE decoder with a lightweight DPT head (Ranftl et al., 2021), GenPercept can infer faster without bearing the performance penalty. For surface normal estimation, the image angular loss brings significant performance improvement thanks to our one-step estimation paradigm.

Qualitative Results. Qualitative visualizations are shown in Fig. 3. We observe excellent generalization of our models in that they can estimate accurate geometric information and promising details not only on diverse real and synthetic scenes, but also on comics, color drafts, and even sketches.

4.2 IMAGE SEGMENTATION

Dichotomous Image Segmentation. This is a category-agnostic, high-quality object segmentation task that accurately separates the object from the background in an image. Consistent with previous methods, we use the six evaluation metrics specified in the DIS task, which include maximal F-measure ($max F_{\beta} \uparrow$) (Achanta et al., 2009), weighted F-measure ($F_{\beta}^w \uparrow$) (Margolin et al., 2014), mean absolute error ($M \downarrow$) (Perazzi et al., 2012), structural measure ($S_{\alpha} \uparrow$) (Fan et al., 2017), mean enhanced alignment measure ($E_{\phi}^m \uparrow$) (Fan et al., 2018; 2021b) and human correction efforts ($HCE_{\gamma} \downarrow$) (Qin et al., 2022). We choose DIS5K (Qin et al., 2022) as the training and testing dataset. We utilize DIS-TR for training and evaluate our model on DIS-VD and DIS-TE subsets. The pixel-wise MSE loss is utilized during training.

Quantitative results of dichotomous image segmentation are shown in Table 8. We only show partial results due to paper page limitations, full comparisons are accessible in the supplementary material. GenPercept outperforms methods like HySM (Nirkin et al., 2021) and IS-Net (Qin et al., 2022) on this challenging dataset across most evaluation metrics, but there exists room for further improvement compared to SoTA methods like MVANet (Yu et al., 2024). As shown in Fig. 5, our approach provides a detailed foreground mask. For thin lines and meticulous objects that are difficult for previous methods to process, our method can also output accurate segmentation results.

Table 8: Quantitative results of dichotomous image segmentation on DIS5K validation and testing sets. Additional cross-dataset evaluation is provided in the supplementary material.

Dataset	DIS-VD						DIS-TE4						Overall DIS-TE (1-4)					
	$max F_{\beta} \uparrow$	$F_{\beta}^w \uparrow$	$M \downarrow$	$S_{\alpha} \uparrow$	$E_{\phi}^m \uparrow$	$HCE_{\gamma} \downarrow$	$max F_{\beta} \uparrow$	$F_{\beta}^w \uparrow$	$M \downarrow$	$S_{\alpha} \uparrow$	$E_{\phi}^m \uparrow$	$HCE_{\gamma} \downarrow$	$max F_{\beta} \uparrow$	$F_{\beta}^w \uparrow$	$M \downarrow$	$S_{\alpha} \uparrow$	$E_{\phi}^m \uparrow$	$HCE_{\gamma} \downarrow$
U ² Net (Qin et al., 2020)	0.748	0.656	0.090	0.781	0.823	1413	0.795	0.705	0.087	0.807	0.847	3653	0.761	0.670	0.083	0.791	0.835	1333
SINetV2 (Fan et al., 2021a)	0.665	0.584	0.110	0.727	0.798	1568	0.699	0.616	0.113	0.744	0.824	3683	0.693	0.608	0.101	0.747	0.822	1411
HySM (Nirkin et al., 2021)	0.734	0.640	0.096	0.773	0.814	1324	0.782	0.693	0.091	0.802	0.842	3331	0.757	0.665	0.084	0.792	0.834	1218
IS-Net (Qin et al., 2022)	0.791	0.717	0.074	0.813	0.856	1116	0.827	0.753	0.072	0.830	0.870	2888	0.799	0.726	0.070	0.819	0.858	1016
MVANet (Yu et al., 2024)	0.904	0.861	0.035	0.909	0.937	878	0.911	0.857	0.041	0.903	0.944	2301	0.916	0.855	0.035	0.905	0.938	790
Our Genpercept	0.857	0.835	0.041	0.87	0.934	1511	0.848	0.829	0.049	0.854	0.938	3799	0.863	0.839	0.039	0.872	0.936	1364
Our Genpercept (infer. at 1024px)	0.877	0.859	0.035	0.887	0.941	1262	0.874	0.858	0.041	0.874	0.947	3321	0.875	0.856	0.036	0.885	0.939	1176

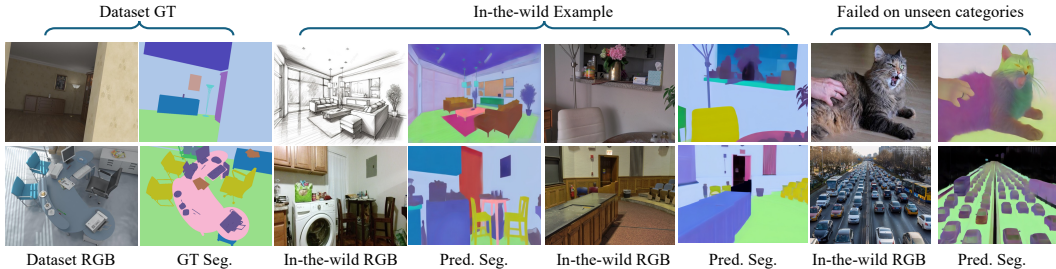


Figure 4: Qualitative results of semantic segmentation in the wild. Trained on the synthetic indoor Hypersim dataset, GenPercept shows much robustness on the trained categories of complex in-the-wild images, e.g., yellow chairs, green floor, and light blue wall. Due to the limited annotation categories and little negative label of “unknown category”, it sometimes fails in outdoor scenes and unseen categories such as cats and cars.

Semantic Image Segmentation. This is a fundamental computer vision task that involves classifying each pixel in an image into a specific category or class. For training, we utilized the indoor synthetic dataset, HyperSim (Roberts et al., 2021), which comprises 40 semantic segmentation class labels. We encode different classes into 3-channel colormaps, treat the task as a regression problem, and fine-tune the original Stable Diffusion with the pixel-wise MSE loss. As demonstrated in Fig. 4, the model generalizes well to classes within the HyperSim annotations, such as chairs and desks, but struggles with unrecognized categories such as cats and cars.

Another choice involves using a customized segmentation head. We incorporate a custom segmentation head, namely UperNet (Xiao et al., 2018b), onto the multi-level features extracted by UNet. For the UperNet segmentation head, we follow the traditional semantic segmentation format to use n-channel output, where n is the number of categories. The quantitative results are presented in Table 9, we test the model’s performance on Hypersim (Roberts et al., 2021) and zero-shot ability on a subset of the ADE20k (Zhou et al., 2017) validation set, which contains overlapping classes. Besides, we compare with Mask2Former (Cheng et al., 2022) by training on ADE20K. GenPercept outperforms ResNet50 (He et al., 2016) and Swin-T (Liu et al., 2021) of Mask2Former but achieves lower performance than Swin-L (Liu et al., 2021).

4.3 IMAGE MATTING

Task Definition. Image matting aims to extract the foreground, background, and alpha mask from an image. Traditional approaches depend on supplementary inputs that delineate foreground, background, and ambiguous areas to reduce uncertainty. Automatic image matting seeks to remove this dependency by directly estimating these components from the image alone. The implementation details can be found in the supplementary material.

Quantitative and Qualitative Results. We evaluate metrics including the sum of absolute differences (SAD), mean squared error (MSE), mean absolute difference (MAD), gradient (Grad.), and Connectivity (Conn.) on the P3M-500-NP test set. SAD and MAD measure the mean L1 distance between predictions and ground truth labels. MSE and CONN focus on L2 distance and connectivity that better reflects human intuition. As shown in Table 10, our GenPercept is less accurate compared

Table 9: Quantitative results of semantic segmentation on Hypersim and ADE20k.

Method	Training Dataset	mIoU↑ (Hypersim)	mIoU↑ (ADE20K)
GenPercept (Train UperNet)	Hypersim	46.0	34.1
GenPercept (Train U-Net + UperNet)		52.9	38.3
Mask2Former R50	ADE20K	-	47.2
Mask2Former Swin-T		-	47.7
Mask2Former Swin-L		-	56.4
GenPercept (Train U-Net + UperNet)		-	50.2

Table 10: Quantitative comparisons of image matting on the P3M-500-NP and AIM500.

Method	Test Dataset	SAD ↓	MAD ↓	MSE ↓	CONN ↓
HATT (Qiao et al., 2020)	P3M-500-NP	30.35	0.0176	0.0072	27.42
SHM (Chen et al., 2018b)		20.77	0.0122	0.0093	17.09
MODNet (Ke et al., 2022)		16.70	0.0097	0.0051	13.81
P3M-Net (Li et al., 2021)		11.23	0.0065	0.0035	12.51
ViTAE-S (Ma et al., 2023)		7.59	0.0044	0.0019	6.96
Our GenPercept		12.77	0.0074	0.0027	10.46
ViTAE-S (Ma et al., 2023)		AIM500	112.52	0.0608	0.0602
Our GenPercept	(Zero-shot)	75.5	0.0444	0.0242	36.74

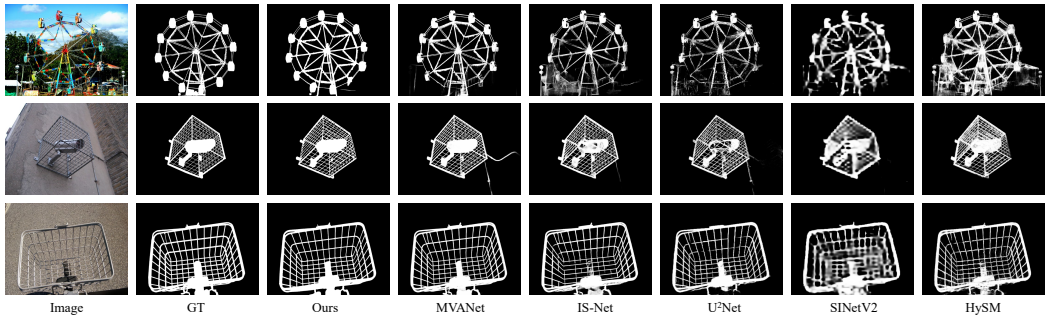


Figure 5: Qualitative comparison of dichotomous image segmentation.

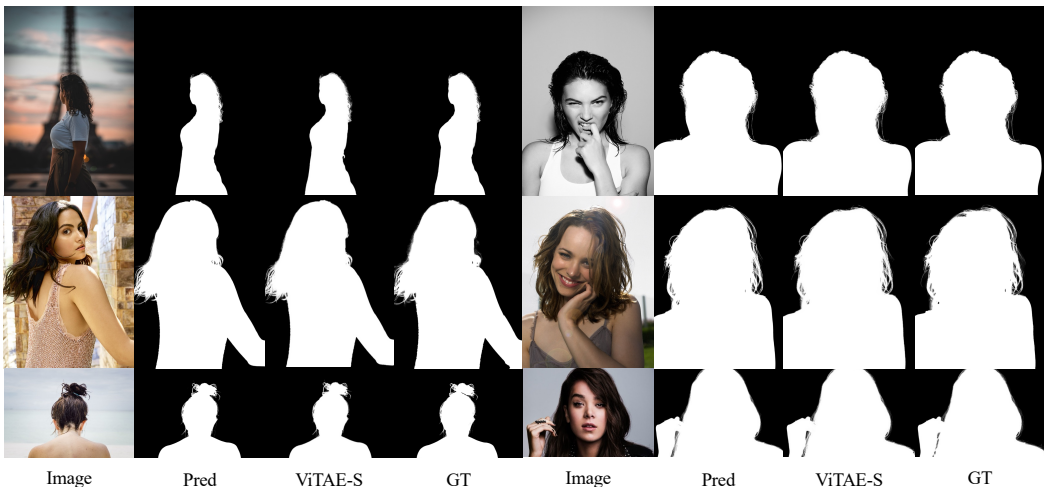


Figure 6: Visualization of image matting on the P3M-500-NP test set.

with the state-of-the-art methods. However, when transferring the human image matting ability to general image matting tasks, GenPercept achieves much better performance. It proves the robustness brought by the prior knowledge of diffusion models pre-trained on the LAION dataset. Quantitative results of image matting are shown in Fig. 6. Please see supplementary for more visualization.

5 RELATED WORK

Vision Pre-Training. Models pretrained on large-scale datasets possess powerful feature extraction capabilities, enabling them to be effectively transferred to a wide range of visual tasks. For instance, the ResNet (He et al., 2016) model pretrained on ImageNet (Russakovsky et al., 2015) can be fine-tuned and applied to perception tasks. By means of contrastive learning, MoCo (He et al., 2020) and CLIP (Radford et al., 2021) acquire rich visual and semantic representations, leveraging their advantages in joint visual and semantic modeling to enhance the performance of multimodal tasks. DINO (Caron et al., 2021), through self-distillation, endows Vision Transformer and convolutional networks with comparable visual representation quality and demonstrates that self-supervised ViT representations contain explicit semantic segmentation information. DINOv2 (Oquab et al., 2024) leverages self-supervised learning on a large curated dataset and exhibits remarkable zero-shot generalization capabilities across computer vision tasks at both image and pixel levels, including classification, semantic segmentation, and depth estimation. In our work, we leverage Stable Diffusion (Rombach et al., 2022) as a prior for scene understanding and transfer it to various perception tasks.

Diffusion Priors for Dense Prediction. Several works explore to use the priors of generative models for perceptual tasks. Some works (Bhattad et al., 2024; Du et al., 2023) demonstrate that generative

models encode property maps of the scene. By finding latent variable offsets, using LoRA (Hu et al., 2022), etc., generative models can directly produce intrinsic images like surface normals, depth, albedo, etc. LDMSeg (Van Gansbeke & De Brabandere, 2024) devises an image-conditioned sampling process, enabling diffusion models to directly output panoptic segmentation. UniGS (Qi et al., 2023) proposes location-aware color encoding and decoding strategies, allowing diffusion models to support referring segmentation and entity segmentation. Marigold (Ke et al., 2024) fine-tunes diffusion model on limited synthetic data, enabling it to support affine-invariant monocular depth estimation and exhibit strong generalization performance. However, Marigold is time-consuming due to the need for multiple iterations of denoising. Additionally, the Gaussian noise leads to inconsistent results across inferences, requiring aggregation over multiple inferences. Xiang et al. (2023) train a denoising auto-encoder for image classification. The difference of their method compared with traditional denoising auto-encoder is that input images are encoded into a latent code and denoising is performed in the latent space rather than the pixel space. They show good results on very small-scale datasets (CIFAR and ImageNet-tiny) to prove the concept and no results were reported on larger datasets. Furthermore, GeoWizard (Fu et al., 2024a) extends the generative capabilities of Marigold, achieving better performance in joint depth and normal estimation, which enhances applications like 3D reconstruction and novel view synthesis. Moreover, DepthFM (Gui et al., 2024) addresses the speed challenge of Marigold by employing flow matching, offering a fast and efficient monocular depth estimation model.

6 CONCLUSION

In this work, we introduce GenPercept, an embarrassingly straightforward yet powerful approach to re-use the off-the-shelf UNet trained using diffusion processes. GenPercept demonstrates the capability to effectively leverage pre-trained diffusion models across a range of downstream dense perception tasks. We contend that our proposed methodology provides an efficient and potent paradigm for harnessing the capabilities of pre-trained diffusion models in dense visual perception tasks.

For future research, we suggest investigating the impact of scaling up the volume of fine-tuning data and exploring the key components of pre-training by applying alternative self-supervised pre-training methods on the LAION dataset, such as Masked Autoencoders (MAE) or Contrastive Language-Image Pretraining (CLIP). It will be helpful to clarify whether the highly detailed visual predictions produced by existing diffusion models are primarily driven by the extensive LAION dataset or the diffusion pretraining paradigm itself.

ACKNOWLEDGMENTS

Y. Ge is with The University of Adelaide and his contribution was made when visiting Zhejiang University. C. Shen is the corresponding author.

A THE FORMULATION OF THREE DIFFERENT PIPELINES

A.1 STOCHASTIC MULTI-STEP GENERATION

For the training process, the RGB image \mathbf{x} and ground-truth label \mathbf{y} are encoded into the latent space with the VAE encoder $\mathbf{z}^{(\mathbf{x})} = \mathcal{E}(\mathbf{x})$, $\mathbf{z}^{(\mathbf{y})} = \mathcal{E}(\mathbf{y})$. The Gaussian noise ϵ is added to the ground-truth label latent $\mathbf{z}^{(\mathbf{y})}$, and the noisy label latent $\mathbf{z}_t^{(\mathbf{y})}$ is concatenated with the clean image latent $\mathbf{z}^{(\mathbf{x})}$ as U-Net input \mathbf{z}_t for each timestep:

$$\begin{aligned} \mathbf{z}_t^{(\mathbf{y})} &= \sqrt{\bar{\alpha}_t} \mathbf{z}^{(\mathbf{y})} + \sqrt{1 - \bar{\alpha}_t} \epsilon, \quad t = [1, \dots, T], \\ \mathbf{z}_t &= \text{concat}(\mathbf{z}_t^{(\mathbf{y})}, \mathbf{z}^{(\mathbf{x})}), \end{aligned} \quad (4)$$

where $\bar{\alpha}_t = \prod_{s=1}^t (1 - \beta_s)$, and β_s is sampled from a variance scheduler $\{\beta_t \in (0, 1)\}_{t=1}^T$. The scheduler is parameters with two hyperparameters β_{start} and β_{end} , which defines the β_t values of $t=0$ and $t=1000$, respectively. For a casual timestep s , β_s is computed by linearly interpolating between $\sqrt{\beta_{start}}$ and $\sqrt{\beta_{end}}$, then squaring each interpolated value. The formulation is as follows.

$$\beta_s = (\sqrt{\beta_{start}} + \frac{s}{T}(\sqrt{\beta_{end}} - \sqrt{\beta_{start}}))^2, \quad s = [1, \dots, T] \quad (5)$$

Then, the denoiser $\mathbf{v}_\theta(\cdot, \cdot)$ is enforced to learn the ‘‘v-prediction’’ (Salimans & Ho, 2021) from a timestep t and the corresponding input \mathbf{z}_t . During training, the parameters of VAE are frozen, and only the denoiser \mathbf{v}_θ is fine-tuned. The timestep is uniformly sampled from 1 to T .

$$\mathcal{L} = \mathbb{E}_{\mathbf{z}^{(\mathbf{y})}, \epsilon \sim \mathcal{N}(0, I), t \sim \mathcal{U}(T)} \left\| (\sqrt{\bar{\alpha}_t} \epsilon - \sqrt{1 - \bar{\alpha}_t} \mathbf{z}^{(\mathbf{y})}) - \mathbf{v}_\theta(\mathbf{z}_t, t) \right\|_2^2. \quad (6)$$

For inference, a Gaussian noise ϵ_t is randomly sampled and denoised step by step with the denoiser $\mathbf{v}_\theta(\cdot, \cdot)$.

$$\begin{aligned} \hat{\mathbf{z}}_T^{(\mathbf{y})} &= \epsilon, \quad \mathbf{z}_t = \text{concat}(\hat{\mathbf{z}}_t^{(\mathbf{y})}, \mathbf{z}^{(\mathbf{x})}), \quad t = [T, \dots, 1], \\ \hat{\mathbf{z}}_{t \rightarrow 0}^{(\mathbf{y})} &= \sqrt{\bar{\alpha}_t} \cdot \hat{\mathbf{z}}_t^{(\mathbf{y})} - \sqrt{1 - \bar{\alpha}_t} \cdot \mathbf{v}_\theta(\mathbf{z}_t, t), \quad \hat{\epsilon}_t = \sqrt{\bar{\alpha}_t} \cdot \mathbf{v}_\theta(\mathbf{z}_t, t) - \sqrt{1 - \bar{\alpha}_t} \cdot \hat{\mathbf{z}}_t^{(\mathbf{y})}, \\ \hat{\mathbf{z}}_{t-1}^{(\mathbf{y})} &= \sqrt{\bar{\alpha}_{t-1}} \cdot \hat{\mathbf{z}}_{t \rightarrow 0}^{(\mathbf{y})} + \sqrt{1 - \bar{\alpha}_{t-1}} \cdot \hat{\epsilon}_t, \quad \hat{\mathbf{y}} = \mathcal{D}(\hat{\mathbf{z}}_{1 \rightarrow 0}^{(\mathbf{y})}). \end{aligned} \quad (7)$$

where the denoising process first computes the estimated noise $\hat{\epsilon}_t$ and the predicted clean latent code $\hat{\mathbf{z}}_{t \rightarrow 0}^{(\mathbf{y})}$ of timestep t from the current latent code $\hat{\mathbf{z}}_t^{(\mathbf{y})}$ and the predicted velocity $\mathbf{v}_\theta(\mathbf{z}_t, t)$. Then, it adds the computed noise $\hat{\epsilon}_t$ back to $\hat{\mathbf{z}}_{t \rightarrow 0}^{(\mathbf{y})}$ to get the latent code of timestep $t - 1$. After repeating it for T times, the predicted clean latent code $\hat{\mathbf{z}}_{1 \rightarrow 0}^{(\mathbf{y})}$ is computed and sent to the VAE decoder \mathcal{D} and estimate the target label $\hat{\mathbf{y}}$. During inference, m randomly sampled noises are introduced to estimate m different predictions, and they are averaged with an ensemble process (Ke et al., 2024) to reduce the randomness of prediction and improve performance.

A.2 DETERMINISTIC MULTI-STEP GENERATION

The inherent random nature of diffusion models makes them challenging to apply to perceptual tasks, which typically aim for accurate results. As a result, existing works have replaced the original Gaussian noise with the target image as RGB noise (Bansal et al., 2024; Lee et al., 2024). Technically, rather than introducing the random Gaussian noise ϵ , we blend the ground-truth label latent $\mathbf{z}^{(\mathbf{y})} = \mathcal{E}(\mathbf{y})$ with the RGB image latent $\mathbf{z}^{(\mathbf{x})} = \mathcal{E}(\mathbf{x})$, which is formulated as:

$$\mathbf{z}_t = \mathbf{z}_t^{(\mathbf{y})} = \sqrt{\bar{\alpha}_t} \mathbf{z}^{(\mathbf{y})} + \sqrt{1 - \bar{\alpha}_t} \mathbf{z}^{(\mathbf{x})}, \quad t = [1, \dots, T], \quad (8)$$

Furthermore, the input latent has been modified to the latent code of input image $\mathbf{z}^{(\mathbf{x})}$ instead of random Gaussian. Consequently, the learning objective function and the inference process are reformulated as follows.

$$\mathcal{L} = \mathbb{E}_{(\mathbf{z}^{(\mathbf{x})}, \mathbf{z}^{(\mathbf{y})}), t \sim \mathcal{U}(T)} \left\| (\sqrt{\bar{\alpha}_t} \mathbf{z}^{(\mathbf{x})} - \sqrt{1 - \bar{\alpha}_t} \mathbf{z}^{(\mathbf{y})}) - \mathbf{v}_\theta(\mathbf{z}_t, t) \right\|_2^2. \quad (9)$$

Table 11: Runtime comparison of three diffusion for perception pipelines on an RTX 4090 GPU.

Experimental Setting	Ensemble	Denoise Steps	Inference Time	GPU Memory
Stochastic Multi-step Generation (w. ensemble)	10	10	~5.74s	16GB
Stochastic Multi-step Generation (w/o ensemble)	1	10	~0.79s	6.95GB
Deterministic Multi-step Generation	1	10	~0.79s	6.95GB
Deterministic One-step Inference (Ours)	1	1	~0.34s	6.95GB
Deterministic One-step Inference + DPT head (Ours)	1	1	~0.24s	6.32GB
Metric3Dv2 (Hu et al., 2024)	1	1	~0.25s	2.63GB
DepthAnythingv2 (Yang et al., 2024b)	1	1	~0.07s	2.82GB
DSINE (Bae & Davison, 2024a)	1	1	~0.18s	2.23GB
Marigold (Ke et al., 2024)	1	10	~0.79s	6.95GB
GeoWizard (Fu et al., 2024b)	1	1	~1.32s	6.81GB
DepthFM (Gui et al., 2024)	1	2	~0.41s	6.97GB
Our GenPercept (DPT head)	1	1	~0.24s	6.32GB

Table 12: The impact of training data volume on affine-invariant monocular depth estimation.

Amount of Data	KITTI		NYU		ScanNet		DIODE		ETH3D	
	AbsRel↓	δ ₁ ↑	AbsRel↓	δ ₁ ↑	AbsRel↓	δ ₁ ↑	AbsRel↓	δ ₁ ↑	AbsRel↓	δ ₁ ↑
90K (1/1)	0.100	0.902	0.053	0.966	0.059	0.961	0.309	0.768	0.068	0.956
45K (1/2)	0.101	0.902	0.056	0.964	0.058	0.963	0.311	0.764	0.070	0.955
22.5K (1/4)	0.109	0.884	0.056	0.963	0.059	0.963	0.322	0.754	0.073	0.950
11.2K (1/8)	0.117	0.866	0.060	0.962	0.065	0.957	0.324	0.753	0.076	0.943
5.6K (1/16)	0.117	0.868	0.063	0.958	0.068	0.952	0.331	0.744	0.084	0.932

$$\begin{aligned}
 \hat{\mathbf{z}}_T^{(\mathbf{y})} &= \mathbf{z}^{(\mathbf{x})}, \quad t = [T, \dots, 1], \\
 \hat{\mathbf{z}}_{t \rightarrow 0}^{(\mathbf{y})} &= \sqrt{\bar{\alpha}_t} \cdot \hat{\mathbf{z}}_t^{(\mathbf{y})} - \sqrt{1 - \bar{\alpha}_t} \cdot \mathbf{v}_\theta(\hat{\mathbf{z}}_t^{(\mathbf{y})}, t), \quad \hat{\mathbf{z}}_t^{(\mathbf{x})} = \sqrt{\bar{\alpha}_t} \cdot \mathbf{v}_\theta(\hat{\mathbf{z}}_t^{(\mathbf{y})}, t) - \sqrt{1 - \bar{\alpha}_t} \cdot \hat{\mathbf{z}}_t^{(\mathbf{y})}, \\
 \hat{\mathbf{z}}_{t-1}^{(\mathbf{y})} &= \sqrt{\bar{\alpha}_{t-1}} \cdot \hat{\mathbf{z}}_{t \rightarrow 0}^{(\mathbf{y})} + \sqrt{1 - \bar{\alpha}_{t-1}} \cdot \hat{\mathbf{z}}_t^{(\mathbf{x})}, \quad \hat{\mathbf{y}} = \mathcal{D}(\hat{\mathbf{z}}_{1 \rightarrow 0}^{(\mathbf{y})}).
 \end{aligned}
 \tag{10}$$

where $\hat{\mathbf{z}}_t^{(\mathbf{x})}$ denotes the predicted RGB noise of timestep t .

A.3 GENPERCEPT: DETERMINISTIC ONE-STEP PERCEPTION

In the main paper, We set the $(\beta_{start}, \beta_{end})$ values to 1, and $\bar{\alpha}_t = \prod_{s=1}^t (1 - \beta_s) = 0$, the formulation of Eq. (8) to Eq. (10) can be greatly simplified as follows.

$$\begin{aligned}
 \mathbf{z}_t &= \mathbf{z}_t^{(\mathbf{y})} = \mathbf{z}^{(\mathbf{x})}, \quad \mathcal{L} = \mathbb{E}_{(\mathbf{z}^{(\mathbf{x})}, \mathbf{z}^{(\mathbf{y})}), t \sim \mathcal{U}(T)} \left\| -\mathbf{z}^{(\mathbf{y})} - \mathbf{v}_\theta(\mathbf{z}_t, t) \right\|_2^2, \\
 \hat{\mathbf{z}}_T^{(\mathbf{y})} &= \mathbf{z}^{(\mathbf{x})}, \quad \hat{\mathbf{z}}_{t-1}^{(\mathbf{y})} = -\hat{\mathbf{z}}_t^{(\mathbf{y})}, \quad \hat{\mathbf{z}}_{1 \rightarrow 0}^{(\mathbf{y})} = -\mathbf{v}_\theta(\hat{\mathbf{z}}_1^{(\mathbf{y})}, t = 1), \quad \hat{\mathbf{y}} = \mathcal{D}(\hat{\mathbf{z}}_{1 \rightarrow 0}^{(\mathbf{y})}).
 \end{aligned}
 \tag{11}$$

One-step prediction. The input of the U-Net is an RGB latent code, and the output becomes the negative value of the ground-truth latent code, with no relationship to the timestep t . Therefore, we set the number of timesteps T to 1 while preserving the same performance.

$$\begin{aligned}
 \mathcal{L} &= \mathbb{E}_{(\mathbf{z}^{(\mathbf{x})}, \mathbf{z}^{(\mathbf{y})})} \left\| -\mathbf{z}^{(\mathbf{y})} - \mathbf{v}_\theta(\mathbf{z}^{(\mathbf{x})}, t = 1) \right\|_2^2, \\
 \hat{\mathbf{z}}_{1 \rightarrow 0}^{(\mathbf{y})} &= -\mathbf{v}_\theta(\mathbf{z}^{(\mathbf{x})}, t = 1), \quad \hat{\mathbf{y}} = \mathcal{D}(\hat{\mathbf{z}}_{1 \rightarrow 0}^{(\mathbf{y})}).
 \end{aligned}
 \tag{12}$$

B A DIFFERENCE BETWEEN IMAGE GENERATION AND VISUAL PERCEPTION

In text-guided image generation, a single textual input can correspond to an immense variety of potential images. This inherent uncertainty makes generating a high-quality image directly from random noise in a single step extremely challenging. Therefore, the multi-step generation enables the model to incrementally remove noise, progressively refining details and textures at each stage, which effectively simplifies the task. However, visual perception tasks conditioned on an RGB image are deterministic without any randomness, and such an easy injective mapping can be estimated with a one-step inference process, as most of the traditional visual perception methods do.

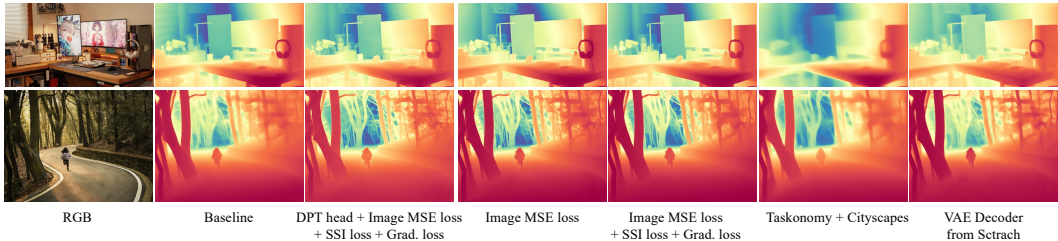


Figure 7: Qualitative visualization of ablation study.

While Marigold series algorithms aim to leverage diffusion models’ ability of generating highly detailed images to enhance visual perception with precise details, reformulating straightforward deterministic tasks as a denoising process can further simplify this problem, enforcing the network to exploit “shortcuts”, as described in Section 3.1 of the main paper and illustrated in Fig. 8.

C RUNTIME ANALYSIS

In this section, we quantitatively analyze the inference times of the three aforementioned pipelines, as summarized in Table 11. The runtime is evaluated by averaging the inference times over 100 images with a resolution of 768×768 , using an RTX 4090 GPU. For “Stochastic Multi-step Generation” methods (Ke et al., 2024; Fu et al., 2024b; Gui et al., 2024), such as Marigold (Ke et al., 2024), they rely on an ensemble process where multiple inferences are performed with varying random noise inputs to mitigate uncertainties introduced by Gaussian noise. Consequently, this approach is computationally expensive. On the other hand, “Deterministic Multi-step Generation” methods (Lee et al., 2024) involve multiple denoising steps, which significantly reduce inference efficiency.

In contrast, our proposed one-step inference paradigm demonstrates a runtime that is 94% and 57% less than those of multi-step methods with ensemble and without ensemble, respectively. Furthermore, by incorporating a customized head, such as the DPT head (Ranftl et al., 2021), both runtime and GPU memory requirements are further reduced by 27% without compromising performance, maintaining a competitive level of accuracy and robustness.

Compared to existing state-of-the-art diffusion-based methods, our proposed GenPercept achieves a notable improvement in inference speed, attributed to the innovative one-step inference paradigm and the customized head. While our method demonstrates inference speeds comparable to Metric3Dv2 (Hu et al., 2024) and DSINE (Bae & Davison, 2024a), it falls behind DepthAnythingV2 (Yang et al., 2024b). Note that the superior performance of DepthAnythingV2 is facilitated by its training on a relatively lightweight model, bolstered by extensive labeled and unlabeled datasets, and supported by substantial computational resources distributed across multiple GPUs.

D THE IMPACT OF DATA VOLUME

With only around 50K Hypersim (Roberts et al., 2021) and 40K Virtual KITTI (Cabon et al., 2020) fine-tuning data, GenPercept can generalize well to diverse tasks and datasets. How much data is needed for transferring at least? We gradually reduce the amount of training data. As shown in Table 12, less training data results in slightly worse performance, but GenPercept still shows much robustness to the data volume.

E MORE VISUALIZATION ANALYSIS

Quantitative Comparisons of Ablations. Visualization of the ablation study experiments in the main paper §2 is shown in Fig. 7. The estimated depth detail remains comparable with a customized “DPT head” (Ranftl et al., 2021). Models trained with lower-quality data like “Taskonomy + Cityscapes” or without the pre-trained VAE decoder parameters suffer from a decline in the abil-

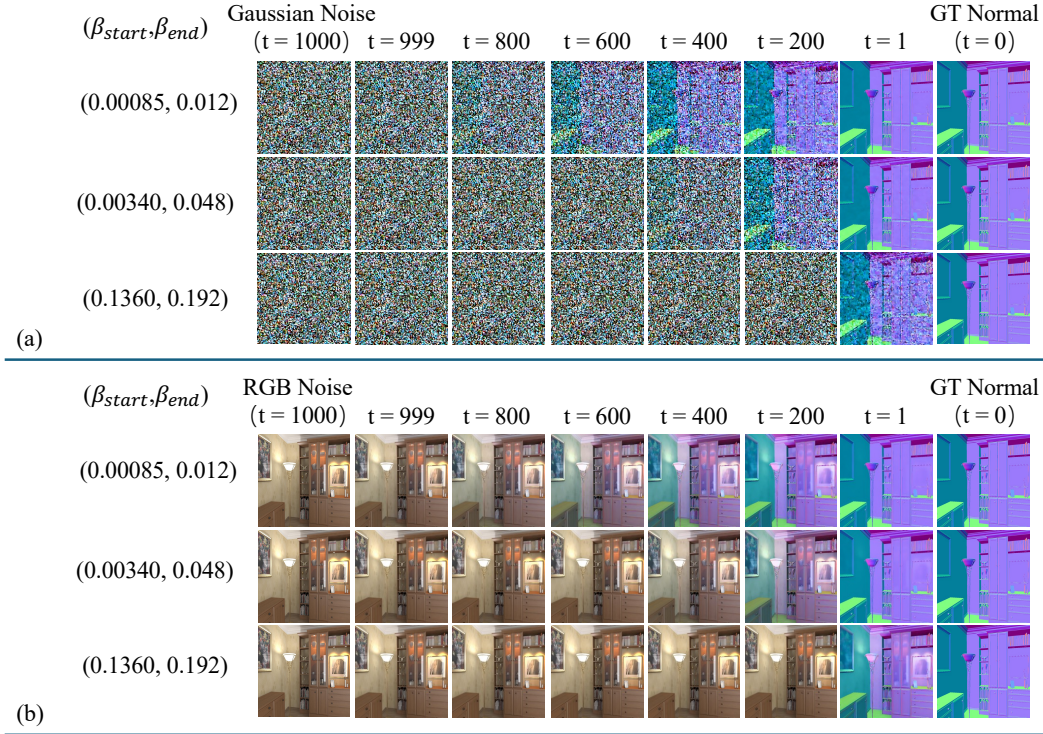


Figure 8: Visualization of different noise forms and proportions in the forward diffusion process.

ity to predict details. We attribute them to the low-quality annotation and the oversized decoder, respectively.

Forward Diffusion Process. More detailed visualization of different noise forms and proportions in the forward diffusion process is shown in Fig. 8. With larger $(\beta_{start}, \beta_{end})$ values of the DDIM scheduler, the proportion of noise will be much higher during the forward diffusion process. When $(\beta_{start}, \beta_{end})$ reaches (1.0, 1.0), the noisy latent will be pure noise latent, which is Gaussian noise and RGB latent for (a) and (b), respectively.

Quantitative Comparisons of Generalization. We compare the generalization performance of models trained on synthetic (50K Hypersim (Roberts et al., 2021) + 40K Virtual KITTI (Capon et al., 2020)) and real data (50K Taskonomy (Zamir et al., 2018) + 40K Cityscapes (Cordts et al., 2016)) for out-of-distribution scenarios. As illustrated in Fig. 9, the robustness of GenPercept trained on real data is comparable to that trained on synthetic data in challenging scenes, such as underwater environments, non-realistic renderings, and evening settings. Notably, models trained on synthetic data demonstrate superior accuracy in estimating transparent objects and capturing geometric details, owing to the high-quality and densely labeled synthetic ground truth.

F AN EXTRA ATTEMPT ON HUMAN POSE ESTIMATION

Task Definition Human Pose Estimation is a task aimed at determining the spatial configuration of a person or object in a given image or video. This involves identifying and predicting the coordinates of particular keypoints.

Implementation Details For human keypoint detection, we use Simple Baseline (Xiao et al., 2018a) for person detection and conduct training on the COCO training set with 15K training samples. Performance is evaluated on the COCO (Lin et al., 2014) validation set. As shown in Fig. 10, it is generalizable to unseen objects in the training set. To evaluate the performance on COCO, we use the customized keypoint head of ViTPose (Xu et al., 2022) for decoding the output. The quantitative results compared with a generalist model, Painter(Wang et al., 2023) is shown in Table 13.

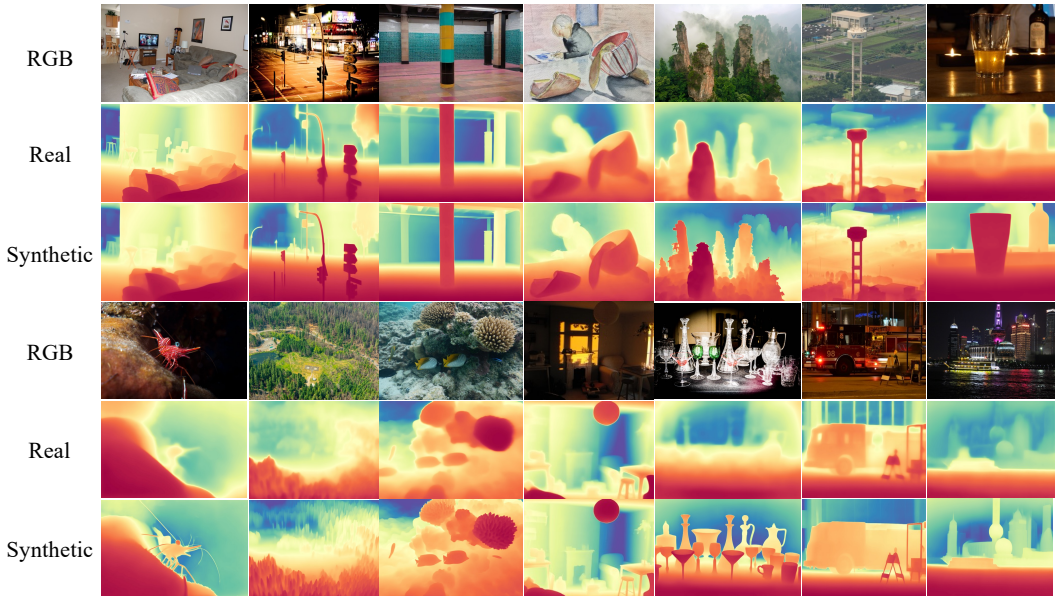


Figure 9: Quantitative comparisons of generalization for models trained on synthetic and real data.

Table 13: Pose estimation on COCO.

Metrics	AP \uparrow	AP .5 \uparrow	AP .75 \uparrow	AP (M) \uparrow	AP (L) \uparrow
Painter (Wang et al., 2023)	0.721	0.900	0.781	0.686	0.786
GenPercept	0.752	0.907	0.824	0.691	0.778

G IMPLEMENTATION DETAILS

Implementation Details of Exploration Experiments in Section 3 of the Main Paper. Unless specified otherwise, we follow Marigold’s training setting and train for 30000 iterations to estimate the affine-invariant monocular depth. The training dataset contains 50K Hypersim (Roberts et al., 2021) images and 40K Virtual KITTI (Cabon et al., 2020) images, and these images are sampled with a sampling rate of 90% for Hypersim and 10% for Virtual KITTI. We freeze the VAE AutoEncoder and fine-tune the U-Net of Stable Diffusion v2.1 to estimate the ground-truth label latent, with a resolution of (480, 640), a batch size of 32, and a learning rate of 3e-5. The multi-resolution noise (Ke et al., 2024) is employed for Gaussian noise and not used for RGB noise (Lee et al., 2024) by default. For inference, the ensemble size and denoising steps are set to 1 and 10, respectively. Evaluation results of absolute relative error (AbsRel) and δ_1 are reported on five unseen monocular depth datasets, including KITTI (Geiger et al., 2013), NYU (Silberman et al., 2012), ScanNet (Dai et al., 2017), DIODE (Vasiljevic et al., 2019), and ETH3D (Schops et al., 2017).

H MORE QUANTITATIVE AND QUALITATIVE EXPERIMENTS

H.1 MONOCULAR DEPTH ESTIMATION

More Qualitative Evaluation. We show the robustness of the monocular depth estimation model in diverse scenes in Fig. 11. Compared to DPT (Ranftl et al., 2021), our Genpercept performs better on estimating details and shows much better robustness even on some sketches. Compared to Marigold (Ke et al., 2024), our method achieves better relative depth visualization.

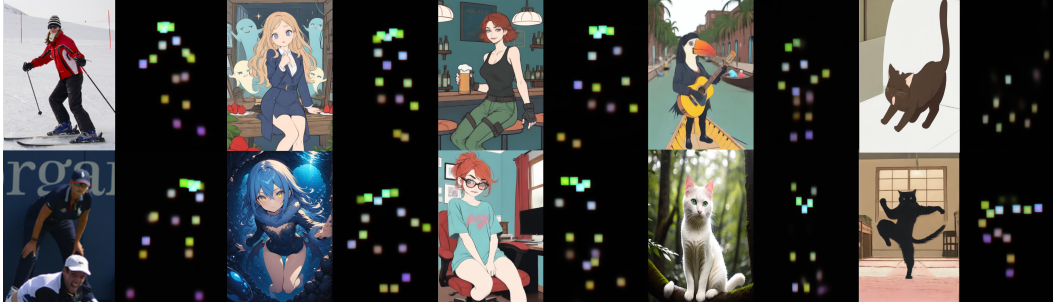


Figure 10: Generalized test results of keypoint detection.

H.2 SURFACE NORMAL ESTIMATION

More Qualitative Evaluation. In Fig. 12, we showcase more qualitative results for the surface normal estimation. DSINE (Bae & Davison, 2024b) is trained on 160K images of 10 datasets, including both real and synthetic data. Our GenPercept is only trained on one synthetic dataset (Hypersim (Roberts et al., 2021)), and can estimate much more detailed surface normal maps.

H.3 DICHOTOMOUS IMAGE SEGMENTATION

More Quantitative Evaluation. To conduct a comprehensive evaluation, we compare our approach with numerous previous models including models for medical image segmentation (Ronneberger et al., 2015), salient object detection (Qin et al., 2019; Zhao et al., 2020; Wei et al., 2020; Chen et al., 2020; Qin et al., 2020), camouflaged object detection (Fan et al., 2021a; Mei et al., 2021), semantic segmentation (Zhao et al., 2017; Chen et al., 2018a; Wang et al., 2020; Yu et al., 2018; Zhao et al., 2018; Howard et al., 2019; Fan et al., 2021c; Nirkin et al., 2021) and models like IS-Net (Qin et al., 2022) and MVANet (Yu et al., 2024) specifically trained for DIS.

As shown in Table 14, our proposed model significantly outperforms methods like IS-Net across most evaluation metrics on this challenging dataset. Compared with MVANet, which inferences with a resolution of 1024×1024 , our GenPercept achieves slightly lower performance, but the results remains competitive and can highlight the effectiveness of our approach for DIS.

Table 14: Quantitative results on DIS5K validation and testing sets.

Dataset	Metric	UNet	BASNet	GateNet	F ³ Net	GCPANet	U ² Net	SINetV2	PFNet	PSPNet	DLV3+	HRNet	BSV1	ICNet	MBV3	STDC	HySM	IS-Net	MVANet	Ours	Ours (1024px)	
DIS-VD	$max F_0 \uparrow$	0.692	0.731	0.678	0.685	0.648	0.748	0.665	0.691	0.691	0.660	0.726	0.662	0.697	0.714	0.696	0.734	0.791	0.904	0.857	0.877	
	$F_0 \uparrow$	0.586	0.641	0.574	0.595	0.542	0.656	0.584	0.604	0.603	0.568	0.641	0.548	0.609	0.642	0.613	0.640	0.717	0.861	0.835	0.859	
	$\bar{M} \downarrow$	0.113	0.094	0.110	0.107	0.118	0.090	0.110	0.106	0.102	0.114	0.095	0.116	0.102	0.092	0.103	0.096	0.074	0.035	0.040	0.035	0.035
	$S_n \uparrow$	0.745	0.768	0.723	0.733	0.718	0.781	0.727	0.740	0.744	0.716	0.767	0.728	0.747	0.758	0.740	0.773	0.813	0.909	0.870	0.887	0.887
	$E_w \uparrow$	0.785	0.816	0.783	0.800	0.765	0.823	0.798	0.811	0.802	0.796	0.824	0.767	0.811	0.841	0.817	0.814	0.856	0.937	0.934	0.941	0.941
	$HCE_s \downarrow$	1337	1402	1493	1567	1555	1413	1568	1606	1588	1520	1560	1660	1503	1625	1598	1324	1116	878	1511	1262	1262
DIS-TE1	$max F_0 \uparrow$	0.625	0.688	0.620	0.640	0.598	0.694	0.644	0.646	0.645	0.601	0.668	0.595	0.631	0.669	0.648	0.695	0.740	0.893	0.841	0.850	
	$F_0 \uparrow$	0.514	0.595	0.517	0.549	0.495	0.601	0.558	0.552	0.557	0.506	0.579	0.474	0.535	0.595	0.562	0.597	0.662	0.823	0.814	0.827	
	$\bar{M} \downarrow$	0.106	0.084	0.099	0.095	0.103	0.083	0.094	0.094	0.089	0.102	0.088	0.108	0.095	0.083	0.090	0.082	0.074	0.037	0.038	0.036	0.036
	$S_n \uparrow$	0.716	0.754	0.701	0.721	0.705	0.760	0.727	0.722	0.725	0.694	0.742	0.695	0.716	0.740	0.723	0.761	0.787	0.879	0.868	0.878	0.878
	$E_w \uparrow$	0.750	0.801	0.766	0.783	0.750	0.801	0.791	0.786	0.791	0.772	0.797	0.741	0.784	0.818	0.798	0.803	0.820	0.911	0.918	0.919	0.919
	$HCE_s \downarrow$	233	220	230	244	271	224	274	253	267	234	262	288	234	274	249	205	149	103	204	165	165
DIS-TE2	$max F_0 \uparrow$	0.703	0.755	0.702	0.712	0.673	0.756	0.700	0.720	0.724	0.681	0.747	0.680	0.716	0.743	0.720	0.759	0.799	0.925	0.876	0.880	
	$F_0 \uparrow$	0.597	0.668	0.598	0.620	0.570	0.668	0.618	0.633	0.636	0.587	0.664	0.564	0.627	0.672	0.636	0.667	0.728	0.874	0.852	0.859	
	$\bar{M} \downarrow$	0.107	0.084	0.102	0.097	0.109	0.085	0.099	0.096	0.092	0.105	0.087	0.111	0.095	0.083	0.092	0.085	0.070	0.03	0.035	0.034	0.034
	$S_n \uparrow$	0.755	0.786	0.737	0.755	0.735	0.788	0.753	0.761	0.763	0.729	0.784	0.740	0.759	0.777	0.759	0.794	0.823	0.915	0.884	0.892	
	$E_w \uparrow$	0.796	0.856	0.804	0.820	0.786	0.833	0.823	0.829	0.828	0.813	0.840	0.781	0.826	0.856	0.834	0.832	0.858	0.944	0.938	0.938	0.938
	$HCE_s \downarrow$	474	480	501	542	574	490	593	567	586	516	555	621	512	600	556	451	340	246	480	410	410
DIS-TE3	$max F_0 \uparrow$	0.748	0.785	0.726	0.743	0.699	0.798	0.730	0.751	0.747	0.717	0.784	0.710	0.752	0.772	0.745	0.792	0.830	0.936	0.885	0.898	
	$F_0 \uparrow$	0.644	0.696	0.620	0.656	0.590	0.707	0.641	0.664	0.657	0.623	0.700	0.595	0.664	0.702	0.662	0.701	0.758	0.89	0.862	0.879	
	$\bar{M} \downarrow$	0.098	0.083	0.103	0.092	0.109	0.079	0.096	0.092	0.092	0.102	0.080	0.109	0.091	0.078	0.090	0.079	0.064	0.031	0.035	0.032	0.032
	$S_n \uparrow$	0.780	0.798	0.747	0.773	0.748	0.809	0.766	0.777	0.774	0.749	0.805	0.757	0.780	0.794	0.771	0.811	0.836	0.92	0.883	0.896	
	$E_w \uparrow$	0.827	0.856	0.815	0.848	0.801	0.858	0.849	0.854	0.843	0.833	0.869	0.801	0.852	0.880	0.855	0.857	0.883	0.954	0.951	0.954	
	$HCE_s \downarrow$	883	948	972	1059	1058	965	1096	1082	1111	999	1049	1146	1001	1136	1081	887	687	512	973	809	809
DIS-TE4	$max F_0 \uparrow$	0.759	0.780	0.729	0.721	0.670	0.795	0.699	0.731	0.725	0.715	0.772	0.710	0.749	0.736	0.731	0.782	0.827	0.911	0.848	0.874	
	$F_0 \uparrow$	0.659	0.693	0.625	0.633	0.559	0.705	0.616	0.647	0.630	0.621	0.687	0.598	0.663	0.664	0.652	0.693	0.753	0.857	0.829	0.858	
	$\bar{M} \downarrow$	0.102	0.091	0.109	0.107	0.127	0.087	0.113	0.107	0.107	0.111	0.092	0.114	0.099	0.098	0.102	0.091	0.072	0.041	0.049	0.041	
	$S_n \uparrow$	0.784	0.794	0.743	0.752	0.723	0.807	0.744	0.763	0.758	0.744	0.792	0.755	0.776	0.770	0.762	0.802	0.830	0.903	0.854	0.874	
	$E_w \uparrow$	0.821	0.848	0.803	0.825	0.767	0.847	0.824	0.838	0.815	0.820	0.854	0.788	0.837	0.848	0.841	0.842	0.870	0.944	0.938	0.947	
	$HCE_s \downarrow$	3218	3601	3654	3760	3678	3653	3683	3803	3806	3709	3864	3999	3690	3817	3819	3331	2888	2301	3799	3321	
Overall DIS-TE(1-4)	$max F_0 \uparrow$	0.708	0.752	0.694	0.704	0.660	0.761	0.693	0.712	0.710	0.678	0.743	0.674	0.711	0.729	0.710	0.757	0.799	0.916	0.863	0.875	
	$F_0 \uparrow$	0.603	0.663	0.590	0.614	0.554	0.670	0.608	0.624	0.620	0.584	0.658	0.558	0.622	0.658	0.628	0.665	0.726	0.855	0.839	0.856	
	$\bar{M} \downarrow$	0.103	0.086	0.103	0.098	0.112	0.083	0.101	0.097	0.095	0.105	0.087	0.110	0.095	0.085	0.094	0.084	0.070	0.035	0.039	0.036	
	$S_n \uparrow$	0.759	0.783	0.732	0.750	0.728	0.791	0.747	0.756	0.755	0.729	0.781	0.737	0.758	0.770	0.754	0.792	0.819	0.905	0.872	0.885	
	$E_w \uparrow$	0.798	0.835	0.797	0.819	0.776	0.835	0.822	0.827	0.819	0.810	0.840	0.778	0.825	0.850	0.832	0.834	0.858	0.938	0.936	0.939	
	$HCE_s \downarrow$	1202	1313	1339	1401	1395	1333	1411	1427	1442	1365	1432	1513	1359	1457	1426	1218	1016	790	1364	1176	

More Qualitative Evaluation. As shown in Fig. 14, our method yields refined segmentation results, providing cleaner foreground masks. It also can produce precise outputs for intricate lines.

Cross Dataset Evaluation. To test the generalization ability of our model, we randomly select some images from other datasets (Agustsson & Timofte, 2017; Lin et al., 2014; Shao et al., 2019) and in-the-wild images for experiments. As shown in Fig. 13, compared to IS-Net and IS-Net-General-Use (Qin et al., 2022), our approach exhibits finer segmentation quality across diverse images, providing cleaner foreground masks. Compared to MVANet (Yu et al., 2024), GenPercept exhibits enhanced robustness when applied to in-the-wild images. This improvement can be attributed to its large-scale pre-training on the LAION dataset and the extensive parameterization of the diffusion model. In contrast, the backbone of MVANet is pre-trained on the ImageNet dataset (Deng et al., 2009), which may limit its performance in more diverse environments.

It is noteworthy that IS-Net-General-Use is fine-tuned on extra datasets to enhance generalization, which indicates that our method has a stronger generalization ability.

H.4 IMAGE MATTING

Implementation Details. We utilize P3M10K (Li et al., 2021), the largest portrait matting dataset with high-resolution portrait images along with high-quality alpha masks to train our model. The training set contains 9,421 high-quality images and annotations and the test set P3M-500-NP is composed of 500 public images from the Internet. We train our GenPercept with pixel-wise MSE loss to further improve the final performance.

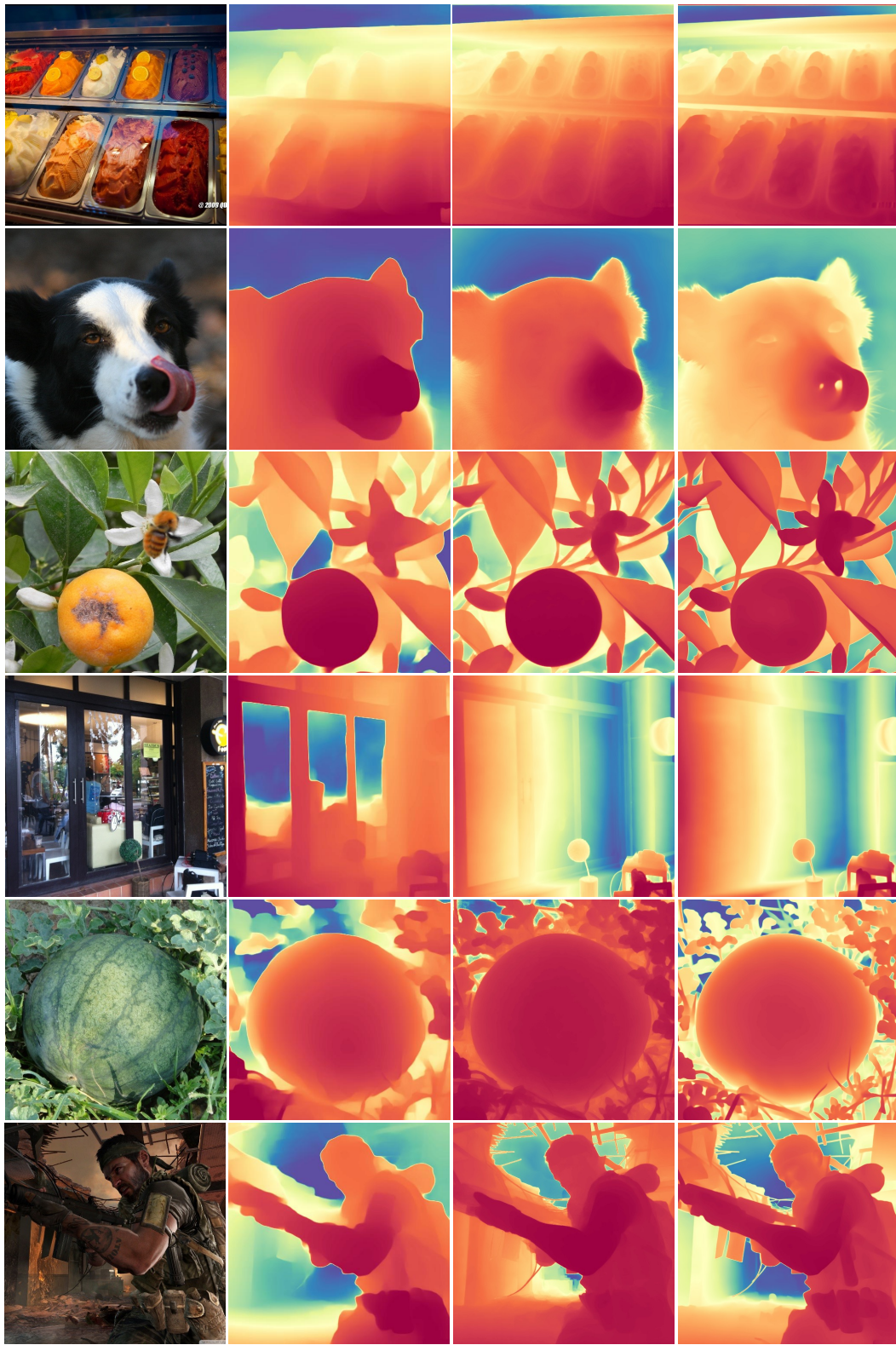
More Qualitative Evaluation. In Fig. 15, we showcase more qualitative results for the image matting task. It is worth noting that our model works well in various resolutions, light environments, human poses, and human orientations. More importantly, our GenPercept model trained on human matting images shows much more robustness to other objects compared to existing P3M10K (Li et al., 2021) SOTA method ViTAE-S (Ma et al., 2023), as illustrated in Fig. 16. It shows that the ViTAE-S overfits the human matting task, while GenPercept preserves the generalization ability. Besides, we also train GenPercept on a more general image matting task on the Composition-1K (Xu et al., 2017) dataset. As shown in Fig. 17, GenPercept shows robustness on more types of objects such as semi-transparent objects, hollow objects, etc.

H.5 IMAGE SEGMENTATION

More Qualitative Evaluation. In Fig. 18, we showcase more qualitative results for the image segmentation task. Our method shows much robustness on the trained categories of complex in-the-wild images. Due to the limited annotation categories and little negative label of “unknown category”, it sometimes fails in outdoor scenes and unseen categories such as cats and cars. Please zoom in for better visualization and more details.

H.6 HUMAN POSE ESTIMATION

More Qualitative Evaluation. In Fig. 19, we showcase more qualitative results for the human pose estimation. We conduct experiments on MHP dataset (Li et al., 2017), and we use mmPose (Contributors, 2020) to render the human pose following the setting of (Bai et al., 2023).



RGB

DPT

Marigold

Ours

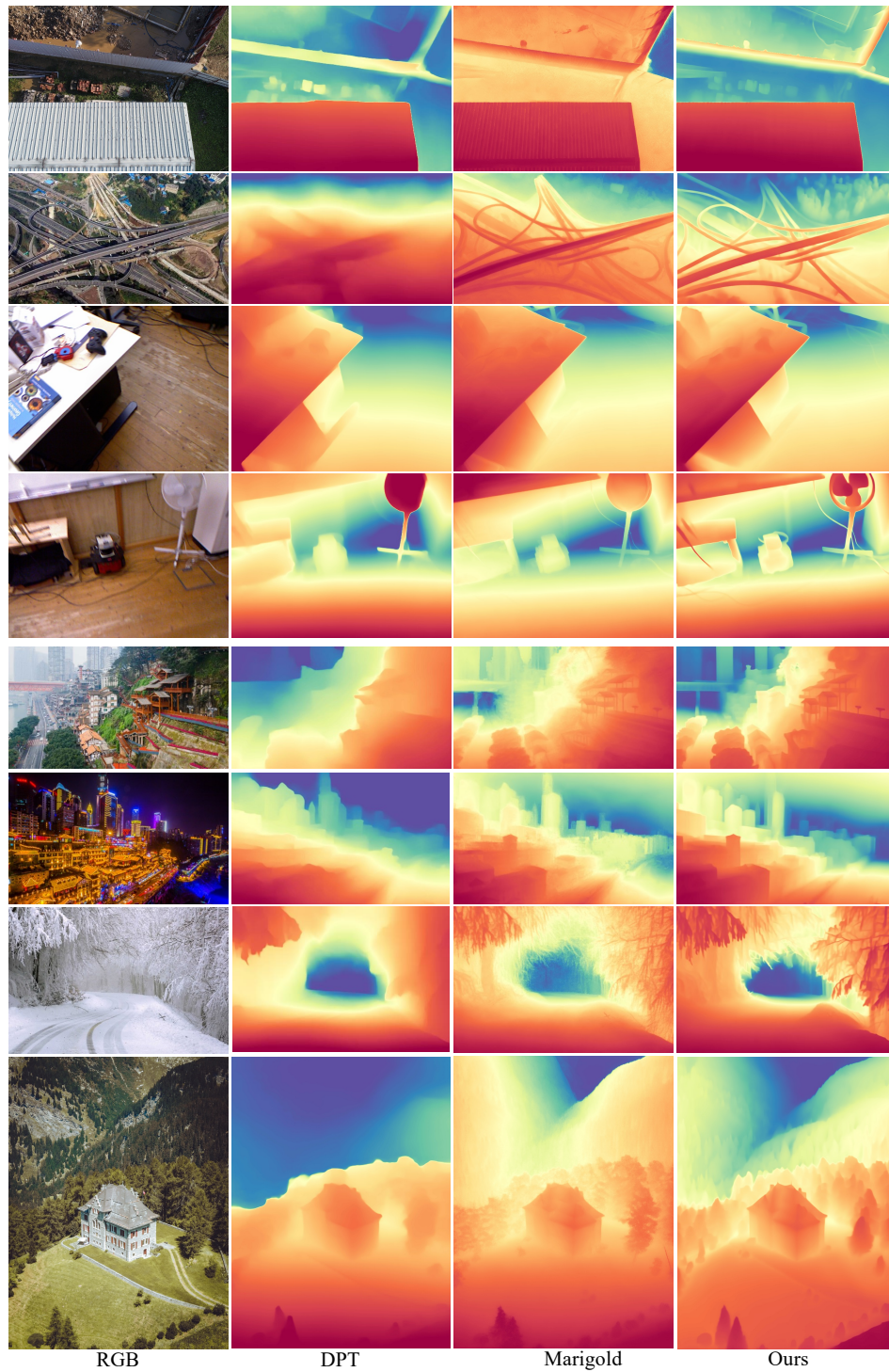
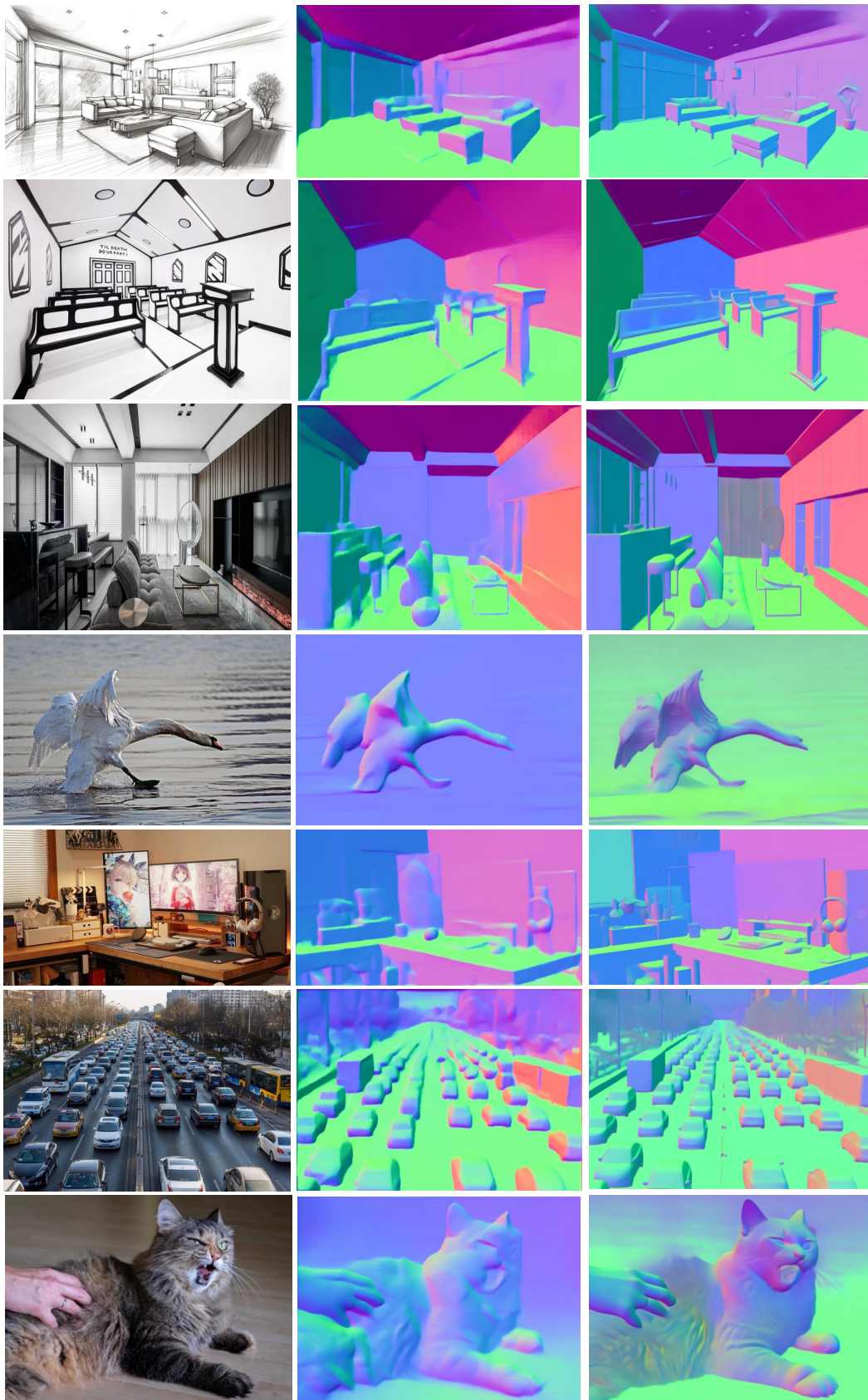


Figure 11: More qualitative results for monocular depth estimation.



RGB

DSINE

Ours

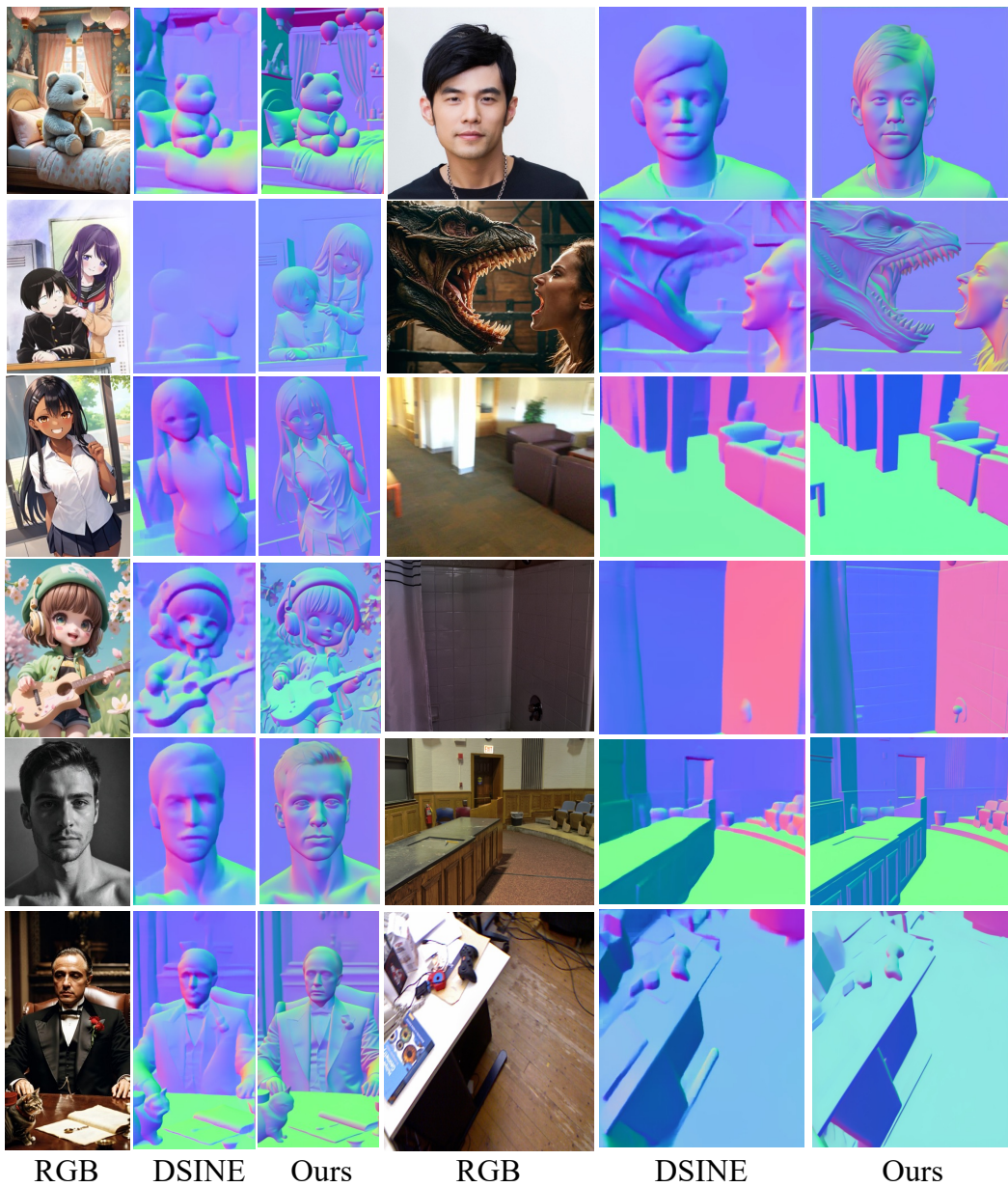
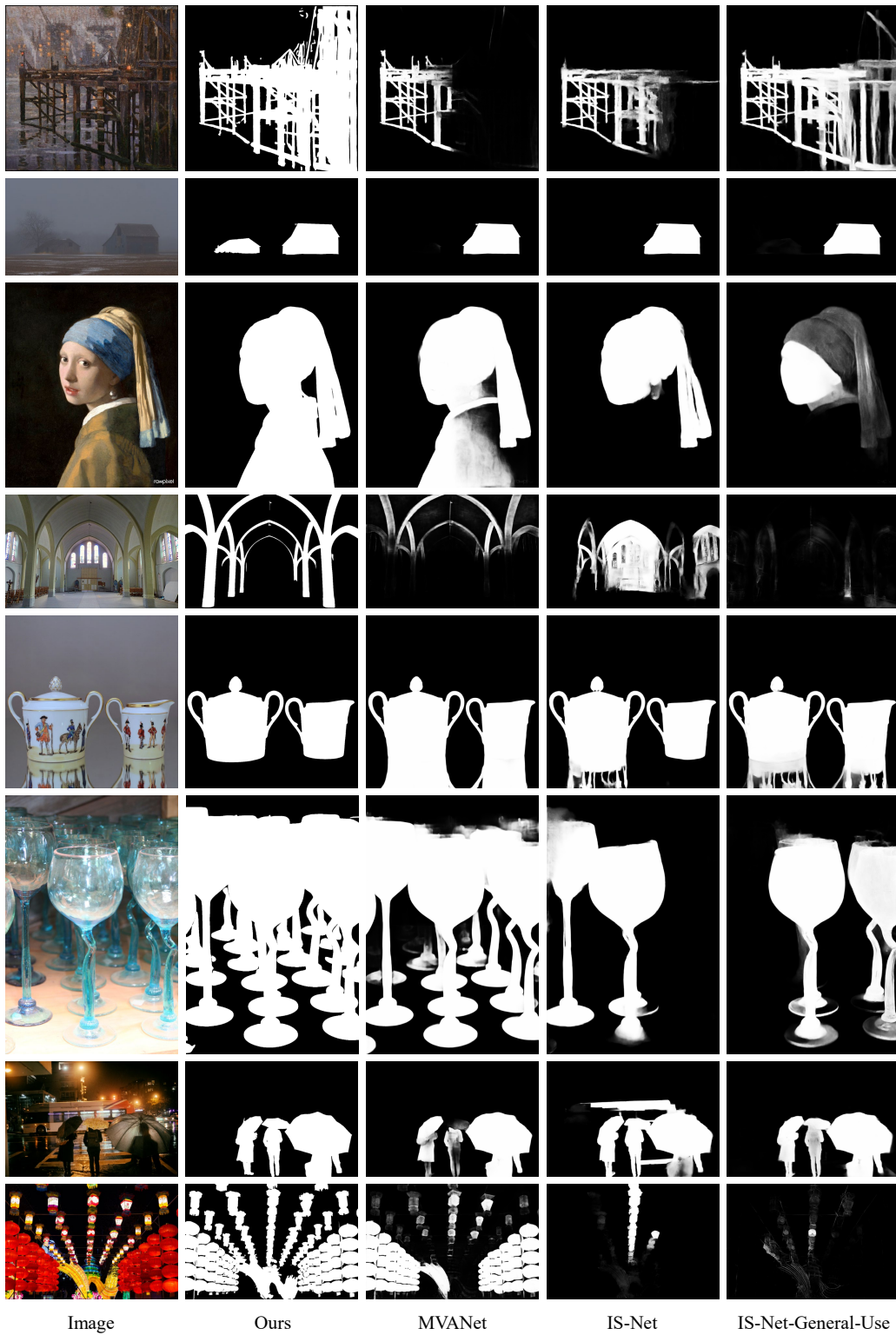


Figure 12: More qualitative comparisons of surface normal estimation. Our GenPercept can achieve more detailed results, even compared to the competitive CVPR2024 method DSINE (Bae & Davison, 2024b). Note that these two visualization coordinate systems are slightly different.



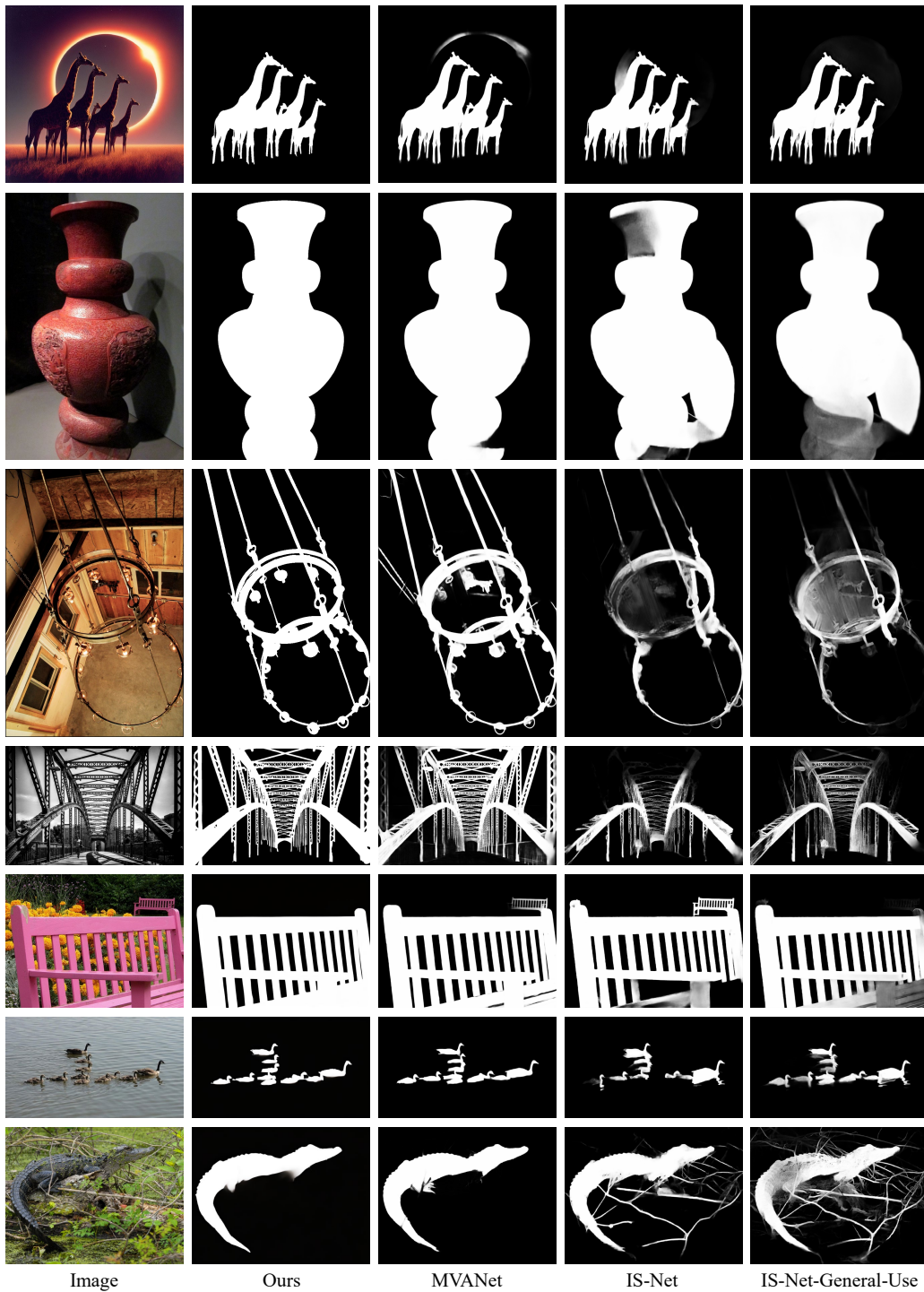


Figure 13: Cross dataset comparison of our model and other models.



Figure 14: Qualitative results of dichotomous image segmentation.

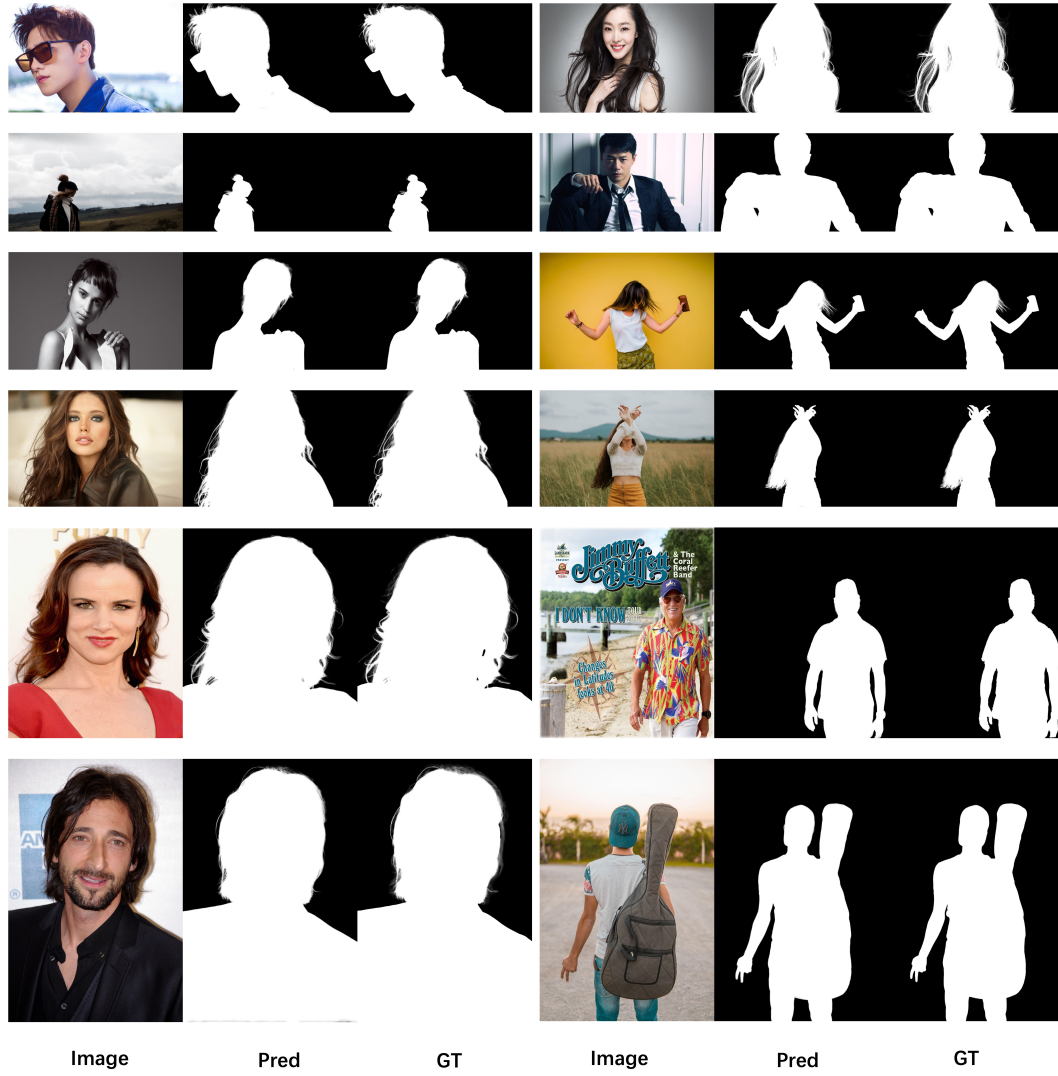
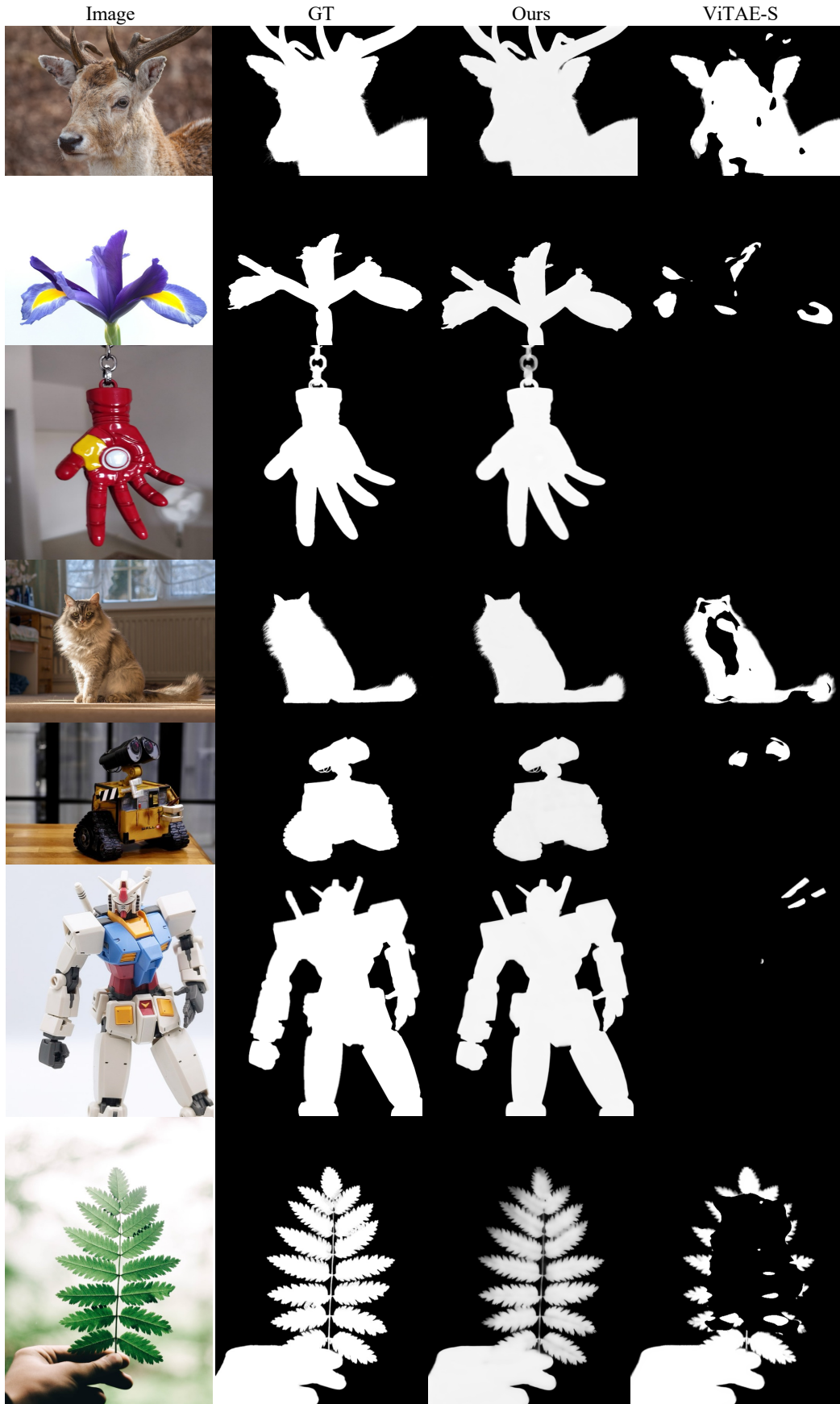


Figure 15: More qualitative results for image matting.



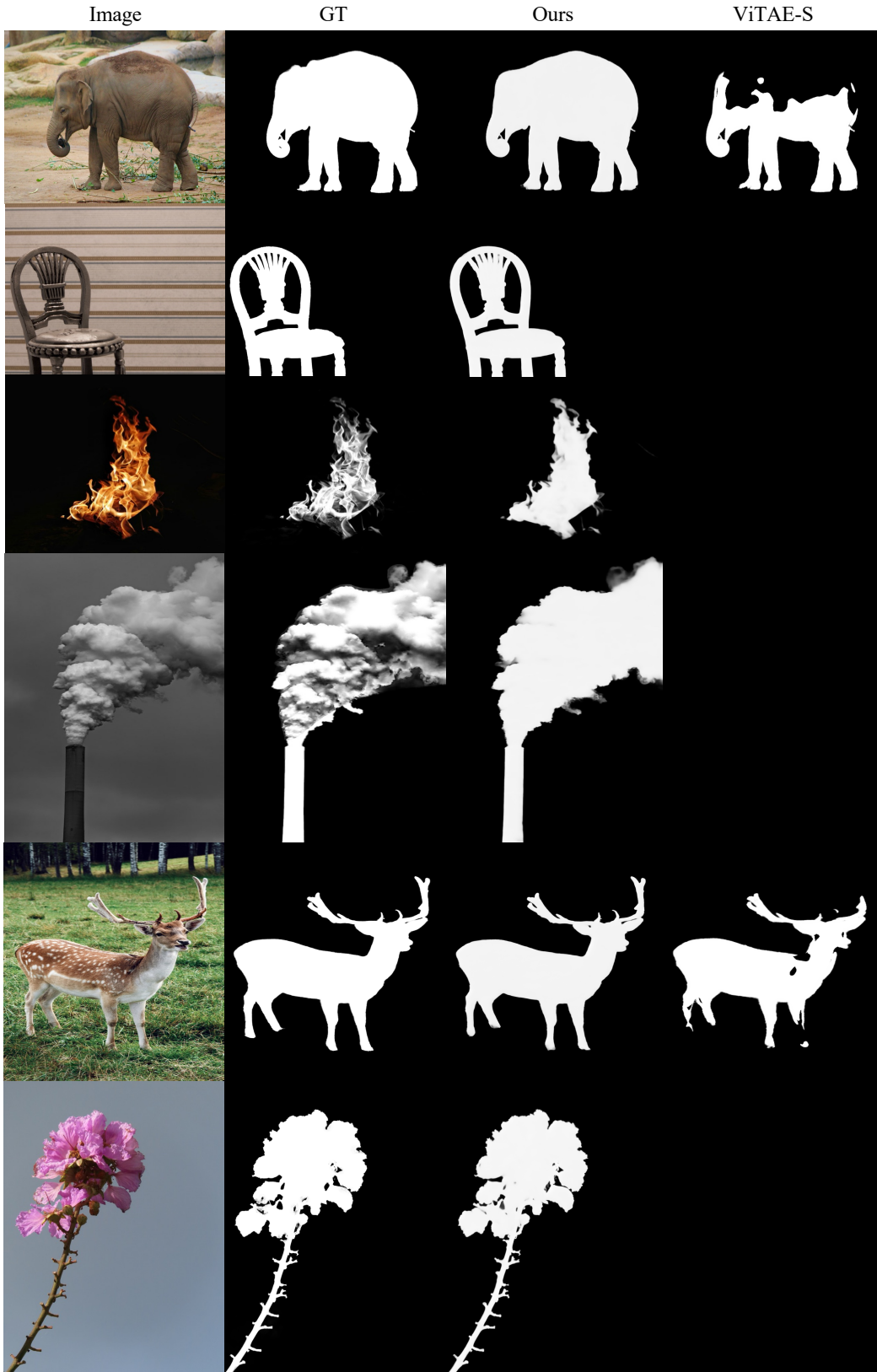


Figure 16: Generalization ability of the human matting model to general image matting images.



Figure 17: More types of image matting such as semi-transparent objects.

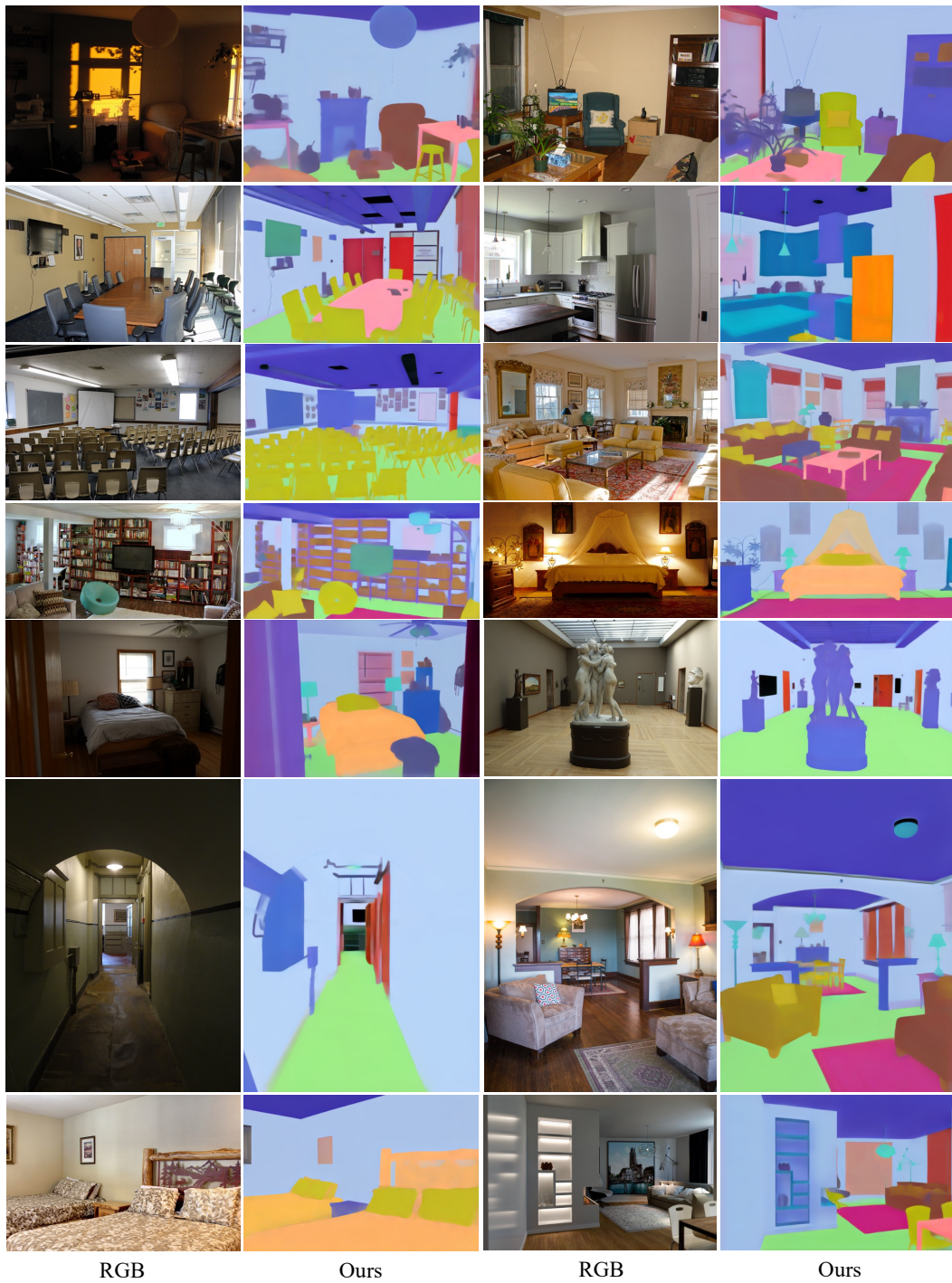


Figure 18: More qualitative results for image segmentation.



Figure 19: More qualitative results for human pose estimation. (Left: original Image, Mid: prediction, Right: ground truth)

REFERENCES

- Radhakrishna Achanta, Sheila Hemami, Francisco Estrada, and Sabine Susstrunk. Frequency-tuned salient region detection. In *Proc. IEEE Conf. Comp. Vis. Patt. Recogn.*, 2009.
- Eirikur Agustsson and Radu Timofte. Ntire 2017 challenge on single image super-resolution: Dataset and study. In *IEEE Conf. Computer Vision and Pattern Recognition Workshops*, 2017.
- Gwangbin Bae and Andrew J Davison. Rethinking inductive biases for surface normal estimation. In *Proc. IEEE Conf. Comp. Vis. Patt. Recogn.*, 2024a.
- Gwangbin Bae and Andrew J Davison. Rethinking inductive biases for surface normal estimation. *arXiv preprint arXiv:2403.00712*, 2024b.
- Yutong Bai, Xinyang Geng, Karttikeya Mangalam, Amir Bar, Alan Yuille, Trevor Darrell, Jitendra Malik, and Alexei A Efros. Sequential modeling enables scalable learning for large vision models. *arXiv: Comp. Res. Repository*, 2023.
- Arpit Bansal, Eitan Borgnia, Hong-Min Chu, Jie Li, Hamid Kazemi, Furong Huang, Micah Goldblum, Jonas Geiping, and Tom Goldstein. Cold diffusion: Inverting arbitrary image transforms without noise. *Proc. Advances in Neural Inf. Process. Syst.*, 2024.
- Anand Bhattad, Daniel McKee, Derek Hoiem, and David Forsyth. Stylegan knows normal, depth, albedo, and more. *Proc. Advances in Neural Inf. Process. Syst.*, 2024.
- D. J. Butler, J. Wulff, G. B. Stanley, and M. J. Black. A naturalistic open source movie for optical flow evaluation. In A. Fitzgibbon et al. (Eds.) (ed.), *Proc. Eur. Conf. Comp. Vis.*, Part IV, LNCS 7577, pp. 611–625. Springer-Verlag, October 2012.
- Yohann Cabon, Naila Murray, and Martin Humenberger. Virtual kitti 2, 2020.

- Mathilde Caron, Hugo Touvron, Ishan Misra, Hervé Jégou, Julien Mairal, Piotr Bojanowski, and Armand Joulin. Emerging properties in self-supervised vision transformers. In *Proc. IEEE Int. Conf. Comp. Vis.*, pp. 9650–9660, 2021.
- Junsong Chen, YU Jincheng, GE Chongjian, Lewei Yao, Enze Xie, Zhongdao Wang, James Kwok, Ping Luo, Huchuan Lu, and Zhenguo Li. Pixart- α : Fast training of diffusion transformer for photorealistic text-to-image synthesis. In *Proc. Int. Conf. Learn. Representations*, 2023.
- Liang-Chieh Chen, Yukun Zhu, George Papandreou, Florian Schroff, and Hartwig Adam. Encoder-decoder with atrous separable convolution for semantic image segmentation. In *Proc. Eur. Conf. Comp. Vis.*, 2018a.
- Quan Chen, Tiezheng Ge, Yanyu Xu, Zhiqiang Zhang, Xinxin Yang, and Kun Gai. Semantic human matting. *arXiv: Comp. Res. Repository*, 2018b.
- Xi Chen, Sida Peng, Dongchen Yang, Yuan Liu, Bowen Pan, Chengfei Lv, and Xiaowei Zhou. Intrinsicanything: Learning diffusion priors for inverse rendering under unknown illumination. *arXiv: Comp. Res. Repository*, 2024.
- Zuyao Chen, Qianqian Xu, Runmin Cong, and Qingming Huang. Global context-aware progressive aggregation network for salient object detection. In *Proc. AAAI Conf. Artificial Intell.*, 2020.
- Bowen Cheng, Ishan Misra, Alexander G Schwing, Alexander Kirillov, and Rohit Girdhar. Masked-attention mask transformer for universal image segmentation. In *Proc. IEEE Conf. Comp. Vis. Patt. Recogn.*, pp. 1290–1299, 2022.
- MMPose Contributors. Openmmlab pose estimation toolbox and benchmark. <https://github.com/open-mmlab/mmpose>, 2020.
- Marius Cordts, Mohamed Omran, Sebastian Ramos, Timo Rehfeld, Markus Enzweiler, Rodrigo Benenson, Uwe Franke, Stefan Roth, and Bernt Schiele. The cityscapes dataset for semantic urban scene understanding. In *Proc. IEEE Conf. Comp. Vis. Patt. Recogn.*, pp. 3213–3223, 2016.
- Angela Dai, Angel X Chang, Manolis Savva, Maciej Halber, Thomas Funkhouser, and Matthias Nießner. Scannet: Richly-annotated 3d reconstructions of indoor scenes. In *Proc. IEEE Conf. Comp. Vis. Patt. Recogn.*, 2017.
- Jia Deng, Wei Dong, Richard Socher, Li-Jia Li, Kai Li, and Li Fei-Fei. Imagenet: A large-scale hierarchical image database. In *arXiv: Comp. Res. Repository*, 2009.
- Xiaodan Du, Nicholas Kolkin, Greg Shakhnarovich, and Anand Bhattad. Generative models: What do they know? do they know things? let’s find out! *arXiv: Comp. Res. Repository*, 2023.
- Ainaz Eftekhari, Alexander Sax, Jitendra Malik, and Amir Zamir. Omnidata: A scalable pipeline for making multi-task mid-level vision datasets from 3d scans. In *Proc. IEEE Int. Conf. Comp. Vis.*, 2021.
- D Fan, M Cheng, Y Liu, T Li, and A Borji. A new way to evaluate foreground maps. In *Proc. IEEE Conf. Comp. Vis. Patt. Recogn.*, 2017.
- Deng-Ping Fan, Cheng Gong, Yang Cao, Bo Ren, Ming-Ming Cheng, and Ali Borji. Enhanced-alignment measure for binary foreground map evaluation. In *Proc. International Joint Conf. Artificial Intelligence*, 2018.
- Deng-Ping Fan, Ge-Peng Ji, Ming-Ming Cheng, and Ling Shao. Concealed object detection. *IEEE Trans. Pattern Anal. Mach. Intell.*, 2021a.
- Deng-Ping Fan, Ge-Peng Ji, Xuebin Qin, and Ming-Ming Cheng. Cognitive vision inspired object segmentation metric and loss function. *Scientia Sinica Informationis*, 2021b.
- Mingyuan Fan, Shenqi Lai, Junshi Huang, Xiaoming Wei, Zhenhua Chai, Junfeng Luo, and Xiaolin Wei. Rethinking bisenet for real-time semantic segmentation. In *Proc. IEEE Conf. Comp. Vis. Patt. Recogn.*, 2021c.

- Xiao Fu, Wei Yin, Mu Hu, Kaixuan Wang, Yuexin Ma, Ping Tan, Shaojie Shen, Dahua Lin, and Xiaoxiao Long. Geowizard: Unleashing the diffusion priors for 3d geometry estimation from a single image. In *Proc. Eur. Conf. Comp. Vis.*, 2024a.
- Xiao Fu, Wei Yin, Mu Hu, Kaixuan Wang, Yuexin Ma, Ping Tan, Shaojie Shen, Dahua Lin, and Xiaoxiao Long. Geowizard: Unleashing the diffusion priors for 3d geometry estimation from a single image. In *Proc. Eur. Conf. Comp. Vis.*, 2024b.
- Andreas Geiger, Philip Lenz, Christoph Stiller, and Raquel Urtasun. Vision meets robotics: The kitti dataset. *Int. J. Robotics Research*, 2013.
- Ming Gui, Johannes S Fischer, Ulrich Prestel, Pingchuan Ma, Dmytro Kotovenko, Olga Grebenkova, Stefan Andreas Baumann, Vincent Tao Hu, and Björn Ommer. Depthfm: Fast monocular depth estimation with flow matching. *arXiv: Comp. Res. Repository*, 2024.
- Kaiming He, Xiangyu Zhang, Shaoqing Ren, and Jian Sun. Deep residual learning for image recognition. In *Proc. IEEE Conf. Comp. Vis. Patt. Recogn.*, 2016.
- Kaiming He, Haoqi Fan, Yuxin Wu, Saining Xie, and Ross Girshick. Momentum contrast for unsupervised visual representation learning. In *Proc. IEEE Conf. Comp. Vis. Patt. Recogn.*, 2020.
- Jonathan Ho, Ajay Jain, and Pieter Abbeel. Denoising diffusion probabilistic models. *Proc. Advances in Neural Inf. Process. Syst.*, 2020.
- Andrew Howard, Mark Sandler, Grace Chu, Liang-Chieh Chen, Bo Chen, Mingxing Tan, Weijun Wang, Yukun Zhu, Ruoming Pang, Vijay Vasudevan, et al. Searching for mobilenetv3. In *Proc. IEEE Int. Conf. Comp. Vis.*, 2019.
- Edward J Hu, Yelong Shen, Phillip Wallis, Zeyuan Allen-Zhu, Yuanzhi Li, Shean Wang, Lu Wang, and Weizhu Chen. LoRA: Low-rank adaptation of large language models. In *Proc. Int. Conf. Learn. Representations*, 2022.
- Mu Hu, Wei Yin, Chi Zhang, Zhipeng Cai, Xiaoxiao Long, Hao Chen, Kaixuan Wang, Gang Yu, Chunhua Shen, and Shaojie Shen. Metric3d v2: A versatile monocular geometric foundation model for zero-shot metric depth and surface normal estimation. *arXiv: Comp. Res. Repository*, 2024.
- Oğuzhan Fatih Kar, Teresa Yeo, Andrei Atanov, and Amir Zamir. 3d common corruptions and data augmentation. In *Proc. IEEE Conf. Comp. Vis. Patt. Recogn.*, 2022.
- Bingxin Ke, Anton Obukhov, Shengyu Huang, Nando Metzger, Rodrigo Caye Daudt, and Konrad Schindler. Repurposing diffusion-based image generators for monocular depth estimation. In *Proc. IEEE Conf. Comp. Vis. Patt. Recogn.*, 2024.
- Zhanghan Ke, Jiayu Sun, Kaican Li, Qiong Yan, and Rynson W.H. Lau. Modnet: Real-time trimap-free portrait matting via objective decomposition. In *Proc. AAAI Conf. Artificial Intell.*, 2022.
- Peter Kocsis, Vincent Sitzmann, and Matthias Nießner. Intrinsic image diffusion for indoor single-view material estimation. In *Proc. IEEE Conf. Comp. Vis. Patt. Recogn.*, pp. 5198–5208, 2024.
- Hsin-Ying Lee, Hung-Yu Tseng, Hsin-Ying Lee, and Ming-Hsuan Yang. Exploiting diffusion prior for generalizable dense prediction. In *Proc. IEEE Conf. Comp. Vis. Patt. Recogn.*, 2024.
- Jianshu Li, Jian Zhao, Yunchao Wei, Congyan Lang, Yidong Li, Terence Sim, Shuicheng Yan, and Jiashi Feng. Multiple-human parsing in the wild. *arXiv preprint arXiv: 1705.07206*, 2017.
- Jizhizi Li, Sihan Ma, Jing Zhang, and Dacheng Tao. Privacy-preserving portrait matting. In *Proc. ACM Int. Conf. Multimedia*, 2021.
- Tsung-Yi Lin, Michael Maire, Serge Belongie, James Hays, Pietro Perona, Deva Ramanan, Piotr Dollár, and C Lawrence Zitnick. Microsoft coco: Common objects in context. In *Proc. Eur. Conf. Comp. Vis.*, 2014.

- Ze Liu, Yutong Lin, Yue Cao, Han Hu, Yixuan Wei, Zheng Zhang, Stephen Lin, and Baining Guo. Swin transformer: Hierarchical vision transformer using shifted windows. In *Proc. IEEE Int. Conf. Comp. Vis.*, pp. 10012–10022, 2021.
- Sihan Ma, Jizhizi Li, Jing Zhang, He Zhang, and Dacheng Tao. Rethinking portrait matting with privacy preserving. *Int. J. Comput. Vision*, 131(8):2172–2197, 2023.
- Ran Margolin, Lihi Zelnik-Manor, and Ayellet Tal. How to evaluate foreground maps? In *Proc. IEEE Conf. Comp. Vis. Patt. Recogn.*, 2014.
- Haiyang Mei, Ge-Peng Ji, Ziqi Wei, Xin Yang, Xiaopeng Wei, and Deng-Ping Fan. Camouflaged object segmentation with distraction mining. In *Proc. IEEE Conf. Comp. Vis. Patt. Recogn.*, 2021.
- Yuval Nirkin, Lior Wolf, and Tal Hassner. Hyperseg: Patch-wise hypernetwork for real-time semantic segmentation. In *Proc. IEEE Conf. Comp. Vis. Patt. Recogn.*, 2021.
- Maxime Oquab, Timothée Darcet, Théo Moutakanni, Huy Vo, and Marc Szafraniec *et al.* DINOv2: Learning robust visual features without supervision. *Trans. Mach. Learn. Research*, 2024.
- Federico Perazzi, Philipp Krähenbühl, Yael Pritch, and Alexander Hornung. Saliency filters: Contrast based filtering for salient region detection. In *Proc. IEEE Conf. Comp. Vis. Patt. Recogn.*, 2012.
- Lu Qi, Lehan Yang, Weidong Guo, Yu Xu, Bo Du, Varun Jampani, and Ming-Hsuan Yang. Unigs: Unified representation for image generation and segmentation. *arXiv: Comp. Res. Repository*, 2023.
- Yu Qiao, Yuhao Liu, Xin Yang, Dongsheng Zhou, Mingliang Xu, Qiang Zhang, and Xiaopeng Wei. Attention-guided hierarchical structure aggregation for image matting. In *Proc. IEEE Conf. Comp. Vis. Patt. Recogn.*, June 2020.
- Xuebin Qin, Zichen Zhang, Chenyang Huang, Chao Gao, Masood Dehghan, and Martin Jagersand. Basnet: Boundary-aware salient object detection. In *Proc. IEEE Conf. Comp. Vis. Patt. Recogn.*, 2019.
- Xuebin Qin, Zichen Zhang, Chenyang Huang, Masood Dehghan, Osmar R Zaiane, and Martin Jagersand. U2-net: Going deeper with nested u-structure for salient object detection. *Pattern Recogn.*, 2020.
- Xuebin Qin, Hang Dai, Xiaobin Hu, Deng-Ping Fan, Ling Shao, and Luc Van Gool. Highly accurate dichotomous image segmentation. In *Proc. Eur. Conf. Comp. Vis.*, 2022.
- Alec Radford, Jong Wook Kim, Chris Hallacy, Aditya Ramesh, Gabriel Goh, Sandhini Agarwal, Girish Sastry, Amanda Askell, Pamela Mishkin, Jack Clark, et al. Learning transferable visual models from natural language supervision. In *Proc. Int. Conf. Mach. Learn.*, 2021.
- René Ranftl, Katrin Lasinger, David Hafner, Konrad Schindler, and Vladlen Koltun. Towards robust monocular depth estimation: Mixing datasets for zero-shot cross-dataset transfer. *IEEE Trans. Pattern Anal. Mach. Intell.*, 2020.
- René Ranftl, Alexey Bochkovskiy, and Vladlen Koltun. Vision transformers for dense prediction. In *Proc. IEEE Int. Conf. Comp. Vis.*, 2021.
- Mike Roberts, Jason Ramapuram, Anurag Ranjan, Atulit Kumar, Miguel Angel Bautista, Nathan Paczan, Russ Webb, and Joshua M. Susskind. Hypersim: A photorealistic synthetic dataset for holistic indoor scene understanding. In *Proc. IEEE Int. Conf. Comp. Vis.*, 2021.
- Robin Rombach, Andreas Blattmann, Dominik Lorenz, Patrick Esser, and Bjorn Ommer. High-resolution image synthesis with latent diffusion models. In *Proc. IEEE Conf. Comp. Vis. Patt. Recogn.*, 2022.
- Olaf Ronneberger, Philipp Fischer, and Thomas Brox. U-net: Convolutional networks for biomedical image segmentation. In *Proc. Medical Image Computing and Computer-Assisted Intervention*, 2015.

- Olga Russakovsky, Jia Deng, Hao Su, Jonathan Krause, Sanjeev Satheesh, Sean Ma, Zhiheng Huang, Andrej Karpathy, Aditya Khosla, Michael Bernstein, et al. Imagenet large scale visual recognition challenge. *Int. J. Comput. Vision*, 115, 2015.
- Tim Salimans and Jonathan Ho. Progressive distillation for fast sampling of diffusion models. In *Proc. Int. Conf. Learn. Representations*, 2021.
- Thomas Schops, Johannes L Schonberger, Silvano Galliani, Torsten Sattler, Konrad Schindler, Marc Pollefeys, and Andreas Geiger. A multi-view stereo benchmark with high-resolution images and multi-camera videos. In *Proc. IEEE Conf. Comp. Vis. Patt. Recogn.*, 2017.
- Shuai Shao, Zeming Li, Tianyuan Zhang, Chao Peng, Gang Yu, Xiangyu Zhang, Jing Li, and Jian Sun. Objects365: A large-scale, high-quality dataset for object detection. In *Proc. IEEE Int. Conf. Comp. Vis.*, 2019.
- Nathan Silberman, Derek Hoiem, Pushmeet Kohli, and Rob Fergus. Indoor segmentation and support inference from rgb-d images. In *Proc. Eur. Conf. Comp. Vis.*, 2012.
- Jiaming Song, Chenlin Meng, and Stefano Ermon. Denoising diffusion implicit models. In *Proc. Int. Conf. Learn. Representations*, 2020.
- Wouter Van Gansbeke and Bert De Brabandere. A simple latent diffusion approach for panoptic segmentation and mask inpainting. *arXiv: Comp. Res. Repository*, 2024.
- Igor Vasiljevic, Nick Kolkin, Shanyi Zhang, Ruotian Luo, Haochen Wang, Falcon Z. Dai, Andrea F. Daniele, Mohammadreza Mostajabi, Steven Basart, Matthew R. Walter, and Gregory Shakhnarovich. DIODE: A Dense Indoor and Outdoor DEpth Dataset. *arXiv: Comp. Res. Repository*, 2019.
- Jingdong Wang, Ke Sun, Tianheng Cheng, Borui Jiang, Chaorui Deng, Yang Zhao, Dong Liu, Yadong Mu, Mingkui Tan, Xinggang Wang, et al. Deep high-resolution representation learning for visual recognition. *IEEE Trans. Pattern Anal. Mach. Intell.*, 2020.
- Xinlong Wang, Wen Wang, Yue Cao, Chunhua Shen, and Tiejun Huang. Images speak in images: A generalist painter for in-context visual learning. In *Proc. IEEE Conf. Comp. Vis. Patt. Recogn.*, 2023.
- Jun Wei, Shuhui Wang, and Qingming Huang. F³net: fusion, feedback and focus for salient object detection. In *Proc. AAAI Conf. Artificial Intell.*, 2020.
- Weilai Xiang, Hongyu Yang, Di Huang, and Yunhong Wang. Denoising diffusion autoencoders are unified self-supervised learners. In *Proc. IEEE Int. Conf. Comp. Vis.*, 2023.
- Bin Xiao, Haiping Wu, and Yichen Wei. Simple baselines for human pose estimation and tracking. In *Proc. Eur. Conf. Comp. Vis.*, 2018a.
- Tete Xiao, Yingcheng Liu, Bolei Zhou, Yuning Jiang, and Jian Sun. Unified perceptual parsing for scene understanding. In *Proc. Eur. Conf. Comp. Vis.*, 2018b.
- Ning Xu, Brian Price, Scott Cohen, and Thomas Huang. Deep image matting. In *Proc. IEEE Conf. Comp. Vis. Patt. Recogn.*, pp. 2970–2979, 2017.
- Yufei Xu, Jing Zhang, Qiming Zhang, and Dacheng Tao. ViTPose: Simple vision transformer baselines for human pose estimation. In *Proc. Advances in Neural Inf. Process. Syst.*, 2022.
- Lihe Yang, Bingyi Kang, Zilong Huang, Xiaogang Xu, Jiashi Feng, and Hengshuang Zhao. Depth anything: Unleashing the power of large-scale unlabeled data. In *Proc. IEEE Conf. Comp. Vis. Patt. Recogn.*, pp. 10371–10381, 2024a.
- Lihe Yang, Bingyi Kang, Zilong Huang, Zhen Zhao, Xiaogang Xu, Jiashi Feng, and Hengshuang Zhao. Depth anything v2. *arXiv: Comp. Res. Repository*, 2024b.
- Chongjie Ye, Lingteng Qiu, Xiaodong Gu, Qi Zuo, Yushuang Wu, Zilong Dong, Liefeng Bo, Yuliang Xiu, and Xiaoguang Han. Stablenormal: Reducing diffusion variance for stable and sharp normal. *arXiv: Comp. Res. Repository*, 2024.

- Wei Yin, Xinlong Wang, Chunhua Shen, Yifan Liu, Zhi Tian, Songcen Xu, Changming Sun, and Dou Renyin. Diversedepth: Affine-invariant depth prediction using diverse data. *arXiv: Comp. Res. Repository*, 2020.
- Wei Yin, Jianming Zhang, Oliver Wang, Simon Niklaus, Long Mai, Simon Chen, and Chunhua Shen. Learning to recover 3d scene shape from a single image. In *Proc. IEEE Conf. Comp. Vis. Patt. Recogn.*, 2021.
- Changqian Yu, Jingbo Wang, Chao Peng, Changxin Gao, Gang Yu, and Nong Sang. Bisenet: Bilateral segmentation network for real-time semantic segmentation. In *Proc. Eur. Conf. Comp. Vis.*, 2018.
- Qian Yu, Xiaoqi Zhao, Youwei Pang, Lihe Zhang, and Huchuan Lu. Multi-view aggregation network for dichotomous image segmentation. In *Proc. IEEE Conf. Comp. Vis. Patt. Recogn.*, pp. 3921–3930, 2024.
- Amir R Zamir, Alexander Sax, William Shen, Leonidas J Guibas, Jitendra Malik, and Silvio Savarese. Taskonomy: Disentangling task transfer learning. In *Proc. IEEE Conf. Comp. Vis. Patt. Recogn.*, pp. 3712–3722, 2018.
- Zheng Zeng, Valentin Deschaintre, Iliyan Georgiev, Yannick Hold-Geoffroy, Yiwei Hu, Fujun Luan, Ling-Qi Yan, and Miloš Hašan. Rgb \leftrightarrow x: Image decomposition and synthesis using material-and lighting-aware diffusion models. In *ACM SIGGRAPH 2024 Conference Papers*, pp. 1–11, 2024.
- Chi Zhang, Wei Yin, Billzb Wang, Gang Yu, Bin Fu, and Chunhua Shen. Hierarchical normalization for robust monocular depth estimation. *Proc. Advances in Neural Inf. Process. Syst.*, 2022.
- Hengshuang Zhao, Jianping Shi, Xiaojuan Qi, Xiaogang Wang, and Jiaya Jia. Pyramid scene parsing network. In *Proc. IEEE Conf. Comp. Vis. Patt. Recogn.*, 2017.
- Hengshuang Zhao, Xiaojuan Qi, Xiaoyong Shen, Jianping Shi, and Jiaya Jia. Icnnet for real-time semantic segmentation on high-resolution images. In *Proc. Eur. Conf. Comp. Vis.*, 2018.
- Xiaoqi Zhao, Youwei Pang, Lihe Zhang, Huchuan Lu, and Lei Zhang. Suppress and balance: A simple gated network for salient object detection. In *Proc. Eur. Conf. Comp. Vis.*, 2020.
- Bolei Zhou, Hang Zhao, Xavier Puig, Sanja Fidler, Adela Barriuso, and Antonio Torralba. Scene parsing through ade20k dataset. In *Proc. IEEE Conf. Comp. Vis. Patt. Recogn.*, 2017.